12-1-2017

Phase equilibria, compressibility, and thermal analysis of bastnaesite-(La)

Richard Lee Rowland
University of Nevada, Las Vegas, oppositeofrick@gmail.com

PHASE EQUILIBRIA, COMPRESSIBILITY, AND THERMAL ANALYSIS OF BASTNAESITE-(LA)

By

Richard L. Rowland II

Bachelor of Science – Geoscience
University of Nevada, Las Vegas
2014

A thesis submitted in partial fulfillment
of the requirements for the

Master of Science – Geoscience

Department of Geoscience
College of Sciences
The Graduate College

University of Nevada, Las Vegas
December 2017

UNLV | GRADUATE COLLEGE

Thesis Approval

The Graduate College
The University of Nevada, Las Vegas

October 26, 2017

This thesis prepared by

Richard L. Rowland II

entitled

Phase Equilibria, Compressibility, and Thermal Analysis of Bastnaesite-(LA)

is approved in partial fulfillment of the requirements for the degree of

Master of Science – Geoscience
Department of Geoscience

Pamela C. Burnley, Ph.D.
Examination Committee Chair

Kathryn Hausbeck Korgan, Ph.D.
Graduate College Interim Dean

Elisabeth M. Hausrath, Ph.D.
Examination Committee Member

Shichun Huang, Ph.D.
Examination Committee Member

Paul Forster, Ph.D.
Graduate College Faculty Representative

Abstract

Understanding basic material properties of rare earth element (REE) bearing minerals such as the temperatures and pressures at which different phases are thermodynamically stable and how they respond to changes in temperature and pressure can assist in understanding how economically viable deposits might form, thereby potentially leading to the discovery of new deposits. Bastnaesite is the most common REE bearing mineral mined. The lanthanum-fluoride end member, bastnaesite-(La), was synthesized. Synthetic bastnaesite-(La) and lanthanum oxyfluoride was investigated using thermal analysis at ambient pressure and high temperature through the methods of thermogravimetric analysis, differential scanning calorimetry, and heated stage powder X-ray diffraction. Bastnaesite-(La)'s thermodynamic behavior from ambient pressure to 11.3 GPa at ambient temperature and from 4.9 to 7.7 GPa up to 400°C temperature was investigated through in-situ single crystal X-ray diffraction in diamond anvil cells. Bastnaesite-(La)'s decomposition reaction to lanthanum oxyfluoride and CO_2 was investigated from ambient pressure to 1.2 GPa and temperatures up to 900°C was investigated in an oven and in a Griggs modified piston cylinder apparatus. A phase diagram illustrating this region of pressure and temperature space was constructed. High temperature X-ray diffraction data were used to fit the Fei thermal equation of state and the thermal expansion coefficient α_{298} for all three materials. Bastnaesite-(La) was fit from 25°C to 450°C (298 K to 723 K) with V_0 = 439.82 Å, α_{298}=4.32×10^{-5} K^{-1}, a_0 = -1.68×10^{-5} K^{-1}, a_1 = 8.34×10^{-8} K^{-1}, and a_2 = 3.126 K^{-1}. Tetragonal γ-LaOF was fit from 450°C to 675°C (723 K to 948 K) with V_0 = 96.51 Å, α_{298} = 2.95×10^{-4} K^{-1}, a_0 = -2.41×10^{-5} K^{-1}, a_1 = 2.42×10^{-7} K^{-1}, and a_2 = 41.147 K^{-1}. Cubic α-LaOF was fit from 674°C to 850°C (973 K to 1123 K) with V_0 = 190.71 Å, α_{298} = -1.12×10^{-5} K^{-1}, a_0 = 2.36×10^{-4} K^{-1}, a_1 = -

1.73×10^{-7} K^{-1}, and a_2 = -17.362 K^{-1}. At ambient temperature, a 3rd-order Birch-Murnaghan equation of state was fit for bastnaesite-(La) with V_o = 439.82 $Å^3$, K_o = 105 GPa, and K' =5.58.

Acknowledgements

This research was sponsored in part by the National Nuclear Security Administration under the Stewardship Science Academic Alliances program through DOE Cooperative Agreement #DE-NA0001982 as well as by National Science Foundation grant EAR-1220548.

This research used resources of the Advanced Photon Source, a U.S. Department of Energy (DOE) Office of Science User Facility operated for the DOE Office of Science by Argonne National Laboratory under Contract No. DE-AC02-06CH11357.

This research used resources and equipment at the National Aeronautics and Space Administration Lyndon B. Johnson Space Center's Astromaterials Research and Exploration Science division.

I owe the largest debt of gratitude to the mentorship and guidance provided by my advisor, Pamela C. Burnley. Without the resources and assistance she provided, I would not likely have been capable of finishing my undergraduate degree, let alone complete any graduate work. Of course, I also could not have completed this work without the support of my committee members: Elisabeth Hausrath, Shichun Huang, and Paul Forster. I was saved from catastrophe numerous times by others from the UNLV Dept. of Geoscience: Joshua Bonde, Jean Cline, Cinch Irwin, Shirin Kaboli, Matthew Lachniet, Rodney Metcalf, Michael Nicholl, Maria Rojas, Elizabeth Smith, Wanda Taylor, Oliver Tschauner, and Michael Wells. Many portions of my research could not have been completed without the expertise or equipment from others: Joanna Clark, Paul Dockweiler, Thomas Hartmann, Barbara Lavina, Ashkan Salamat, and Brad Sutter. My mentors, colleagues, and friends at JETS/NASA JSC were also key players in finishing this research: Lisa Danielson, Kathleen Vander Kaaden, and Kellye Pando. Many friends and

colleagues also had significant impact on my success: Candace Bracken, Christopher Cline, Adela Fernandez, Raina Gaddis, Brandon Guttery, Less Hess, Zachary Jensen, Daniel Mast, Evan Mohr, Katie Peterson, Nolan Regis, Justin Reppart, Dawn Reynoso, Kat Sauer, Devon Smith, Heather Stoller, Amber Turner, Katy Wilson, and many others. And of course, last but not least, I could never have made it this far without the love and support of my family: Rick Sr., Donella, Rebbecca, Peter, Zoe Jean, Norman, and Dorothy Jean. To everyone here, and to those that I shouldn't have forgotten to add to the list (but I must have missed a few!) thank you, I am eternally grateful.

Table of Contents

List of Tables

List of Figures

Chapter 1 – Background

The rare earth elements (REEs) are a collection of elements comprised of the lanthanides and yttrium, and are often separated into the light rare earth elements (LREEs) – lanthanum, cerium, praseodymium, neodymium, samarium, and europium, and the heavy rare earth elements (HREEs) – yttrium, gadolinium, terbium, dysprosium, holmium, erbium, thulium, ytterbium, and lutetium. Despite the word "rare" in their title, the REEs are more common in the Earth's crust than noble metals like gold or platinum, and some are more common than base metals like lead (Long et al., 2010). This collection of elements obtains its reputation for rarity because they are generally only found as trace impurities in most minerals, and are very rarely found as cations in their own minerals. Even more rarely are those minerals found in deposits with high enough concentration to be economically viable (Castor, 2008a; Chen, 2011).

We mine and use several orders of magnitude larger quantities of both the noble and base metals than we do of the REEs, but they are still critical to the health of the economy. Unique electronic and magnetic properties manifest in the REEs and their compounds due to partially filled f-block orbitals. Because of this, they are uniquely suited for many different applications including (but not limited to) magnets, electric motors, batteries, phosphors for displays and lighting, catalysts for petroleum refinement, other electronic components, ceramics, optical components, polishing compounds, and pigments (Castor, 2008b; Long et al., 2010).

Bastnaesite is the mineral mined for REEs at both Bayan Obo in China and Mountain Pass in California, which are two of the largest producers of LREEs in the world. Having the general formula of $(Ce,La,Y)CO_3(F,OH)$, bastnaesite hosts LREEs. It occurs mainly in carbonatites and is usually found in association with calcite, dolomite, and barite, but has also been discovered in

metamorphic rocks in the garnet stability zone. Both Bayan Obo and Mountain Pass are carbonatite deposits (Savko and Bazikov, 2011; Long et al., 2010; Castor, 2008b, 2008a; Chen, 2011).

Over 90% of the current supply of LREEs is controlled by China, with most of the rest of the supply being produced as byproducts from the mining of other materials, presenting the potential for a supply problem. Molycorp's Mountain Pass mine in the United States was the leading producer of REEs in the world from the 1960s until the 1990s, when China's Bayan Obo mine took over as the primary supplier (Chen, 2011; Castor, 2008a; Long et al., 2010). Therefore, discovering improved exploration methods for this mineral is an important step towards preventing potential supply disruptions which would negatively affect the economy.

Understanding basic material properties such as phase equilibria, equations of state, and the crystallographic structure of bastnaesite can assist in understanding the formation of these mineral deposits and thereby assist in locating new deposits. This research project will focus on the lanthanum-fluoride end member, bastnaesite-(La) ($LaCO_3F$). End members with different REE cations may behave differently with variations in the redox environments; some REEs (such as cerium) have alternative valence states from the 3+ charge necessary for bastnaesite. Lanthanum only exhibits a 3+ charge, and the fluoride (F^-) anion is the most common species of bastnaesite found in nature, with the hydroxide (OH^-) anion usually being found only in altered or weathered samples (Donnay and Donnay, 1953; Oftedal, 1931; Glass and Smalley, 1945; Castor, 2008a, 2008b; Yang et al., 2008). By exploring the phase equilibria of a single end member of the system, we can begin to put constraints on the pressure and temperature conditions favorable for the formation of these REE deposits. Further studies of other end-members of bastnaesite will help to constrain or expand feasible pressures and temperatures for REE mineralization in this system.

The behavior of bastnaesite under high pressure and high temperature conditions has not been studied; all previous experimental work has been at or below 0.1 GPa (Hsu, 1992). While this is appropriate in the case of natural occurrences of bastnaesites at Mountain Pass where the deposit is interpreted to have formed at depths between three and five kilometers, the parental magma is attributed to a mantle source (Castor, 2008b). The parental magma is interpreted to have been an ultrapotassic mafic intrusion from which a carbonatite melt exsolved. Bastnaesite crystallized directly from this melt along with the associated calcite, dolomite, and barite. Thus, understanding the high pressure behavior of the material is important in order to determine if bastnaesite only forms at shallow depths or if it can form closer to the source of the parental magma.

Bastnaesite-(La)-LaOF-CO_2 system

Bastnaesite-(La) ($LaCO_3F$) exhibits hexagonal symmetry in the P-62c space group with six formula units of alternating layers of carbonate and layers of lanthanum and fluorine (Donnay and Donnay, 1953; Oftedal, 1931; Ni et al., 1993). In response to the application of sufficient heat, bastnaesite-(La) decomposes via the decarbonation reaction $LaCO_3F$ + (heat) = LaOF + CO_2. At ambient conditions, γ-LaOF exhibits tetragonal symmetry in the P4/nmm space group with two formula units per unit cell (Woo et al., 2013; Jacob et al., 2006; Fergus and Chen, 2000; Shinn and Eick, 1969; Zachariasen, 1951). At high temperature, α-LaOF is stable with cubic symmetry in the Fm3m space group with four formula units per unit cell (Pistorius, 1973; Klemm and Klein, 1941; Mathews et al., 1997; Achary et al., 1998; Holtstam et al., 2004). β-LaOF is reported as stable at ambient pressure and temperature exhibiting rhombohedral symmetry in the R-3m space group

with six formula units per unit cell (Achary et al., 1998; Woo et al., 2013; Zachariasen, 1951), but this structure was not encountered during this investigation.

Previous studies on bastnaesite

Williams-Jones and Wood (1992) constructed a low pressure (<100MPa) petrogenetic grid for several different fluorocarbonates below 800°C based upon published experiments by others. Bastnaesite has been interpreted to be potentially useful as an index mineral in some low temperature, low pressure greenschist facies rocks where it is suspected to react with apatite to form monazite at the highest temperature portion of the garnet zone (Savko and Bazikov, 2011).

Methods for synthesizing bastnaesite have been explored from room pressure up to 100 MPa and at temperatures from ambient to >800°C. Several methods use hydrofluoric acid which can be difficult to handle safely (Haschke, 1975; Hsu, 1992; Janka and Schleid, 2009; Pradip et al., 2013).

Low pressure (< 0.1 GPa) work was conducted exploring the thermal decomposition of bastnaesite-(La), bastnaesite-(Ce), and their (OH) analogs at temperatures between 400°C and 900°C in a cold-seal vessel (Hsu, 1992). The results from room pressure experiments combined with 100 MPa pressurized experiments give only a shallow, straight line slope for the phase boundary between bastnaesite and the decomposition products: a solid oxide phase and CO_2 gas.

The ambient pressure crystallography of natural bastnaesites has been studied (Oftedal, 1931; Glass and Smalley, 1945; Donnay and Donnay, 1953; Ni et al., 1993) to determine the hexagonal and layered nature of the structure, but the materials studied were solid solutions of the Ce and La varieties, not endmembers. The structure of hydroxyl-bastnaesite-(Ce) was studied with X-ray diffraction and Raman spectroscopy (Yang et al., 2008), and was determined to be slightly

different than the fluorcarbonate structure. While both structures are hexagonal, with alternating layers of carbonate ions and REE anions, in the hydroxyl-bastnaesite structure the carbonate ions sit at different angles and at different distances from each other.

The isobaric heat capacity and enthalpy of formation have been measured on natural bastnaesite-(Ce) via differential scanning calorimetry and thermogravimetric analysis (Gysi and Williams-Jones, 2015). The enthalpies of formation for several synthetic hydroxyl and fluorcarbonate bastnaesites have been measured using high temperature oxide melt solution calorimetry (Shivaramaiah et al., 2016).

Thermal Expansion

The change in volume of a material due to changes in thermodynamic state variables, such as temperature or pressure, affects the change of free energy of the material, which determines whether the material is stable. Thermal expansion describes the change of volume or length of a material at fixed pressure with respect to changes in temperature, and is defined in terms of the thermal expansion coefficient α:

$$\alpha = \frac{1}{V}\left(\frac{\partial V}{\partial T}\right)_P$$

where V is the volume, P is the pressure, and T is the temperature. For most measurements over limited ranges of temperatures, it can be described by the polynomial:

$$\alpha(T) = a_0 + a_1 T + a_2 T^{-2}$$

where α is the mean thermal expansion coefficient, T is the measured temperature and a_0, a_1 and a_2 are constants fit from experimental data. For most solids at ambient pressure, the thermal equation of state:

$$V(T) = V_0 \times e^{\left[a_0(T-298)+\frac{1}{2}a_1(T^2-298^2)+a_2\left(\frac{1}{T}-\frac{1}{298}\right)\right]}$$

allows the calculation of the high temperature volume at ambient pressure, where V_0 is the volume at a reference temperature (298 K) and T is the measured temperature in Kelvin (Fei, 1995).

Compressibility

Compressibility of a material can be described by an isothermal equation of state. The third order Birch-Murnaghan equation of state (Birch, 1947) describes a material's change in volume as a response to a change in hydrostatically applied pressure at a fixed temperature. It is represented by:

$$P(V_m) = \frac{3K_o}{2}\left[\left(\frac{V_o}{V_m}\right)^{\frac{7}{3}} - \left(\frac{V_o}{V_m}\right)^{\frac{5}{3}}\right] \times \{1 + \frac{3}{4}(K' - 4)[(\frac{V_o}{V_m})^{\frac{2}{3}} - 1]\}$$

Where P is hydrostatically applied pressure, V_m is the measured unit cell volume, and V_o is the unit cell volume measured at ambient pressure and temperature. K_o is the bulk modulus that describes a materials resistance to compression, which is the ratio of the change in pressure to the reduction in volume and is represented by the expression:

$$K_o = -V(\frac{\partial P}{\partial V})_P$$

K’ is the first derivative of the bulk modulus. For many materials at pressures below ~10 GPa, it is acceptable to assume a value of K’=4, which reduces the Birch-Murnaghan equation of state to its 2nd order form of:

$$P(V_m) = \frac{3K_o}{2}\left[\left(\frac{V_o}{V_m}\right)^{\frac{7}{3}} - \left(\frac{V_o}{V_m}\right)^{\frac{5}{3}}\right]$$

For many materials that only experience crustal conditions, this form is adequate to describe their behavior.

Manuscripts

The following chapters describe the different methods used to measure physical properties and explore equilibrium chemistry in the bastnaesite-(La) system and are presented in manuscript form. Chapter two details the exploration of thermal expansion and phase changes at ambient pressure utilizing thermogravimetric analysis, differential scanning calorimetry, and heated X-ray diffraction. Chapter three details the experimental exploration of compressibility and fitting of an equation of state for bastnaesite-(La) utilizing the diamond anvil cell. Chapter four describes the experimental exploration of phase equilibria with a fixed composition and the variables of pressure and temperature utilizing a piston cylinder apparatus.

Chapter 2 – Thermal expansion and decomposition of bastnaesite-(La) to lanthanum oxyfluoride at ambient pressure from 278 K to 1173 K

Abstract

Understanding basic material properties of rare earth element (REE) bearing minerals such as the temperatures at which different phases are thermodynamically stable and how they respond to changes in temperature can assist in understanding how economically viable deposits might form, thereby potentially leading to the discovery of new deposits. Bastnaesite is the most common REE bearing mineral mined. The lanthanum-fluoride end member, bastnaesite-(La), was synthesized and the thermal behavior and its decomposition products from 298 K to 1173 K were explored under ambient pressure conditions through thermogravimetric analysis, differential scanning calorimetry, and heated powder X-ray diffraction. At ambient pressure, bastnaesite-(La) is stable up to 598 K, where it decomposes into CO_2 and tetragonal γ-LaOF. Above 948 K, cubic α-LaOF is stable. High temperature X-ray diffraction data were used to fit the Fei thermal equation of state and the thermal expansion coefficient α_{298} for all three materials. Bastnaesite-(La) was fit from 298 K to 723 K with V_0 = 439.82 Å, α_{298}=4.32×10^{-5} K^{-1}, a_0 = -1.68×10^{-5} K^{-1}, a_1 = 8.34×10^{-8} K^{-1}, and a_2 = 3.126 K^{-1}. Tetragonal γ-LaOF was fit from 723 K to 948 K with V_0 = 96.51 Å, α_{298} = 2.95×10^{-4} K^{-1}, a_0 = -2.41×10^{-5} K^{-1}, a_1 = 2.42×10^{-7} K^{-1}, and a_2 = 41.147 K^{-1}. Cubic α-LaOF was fit from 973 K to 1123 K with V_0 = 190.71 Å, α_{298} = -1.12×10^{-5} K^{-1}, a_0 = 2.36×10^{-4} K^{-1}, a_1 = -1.73×10^{-7} K^{-1}, and a_2 = -17.362 K^{-1}.

Introduction

Rare earth elements (REE), the elements with atomic number 57 to 71, are the first on the periodic table to begin populating F-block orbitals. Because of this, they exhibit unique electronic properties and thus are sought after for various technological applications for which other metals are not suitable. They are considered rare, not because of their relative abundance in the Earth's crust, but because they are generally only found as trace impurities instead of primary cations in minerals. Relative crustal abundances of REEs are higher than noble metals such as gold or platinum, and some REEs are more common than base metals like lead. The limited number of minerals that do form with high REE content are rarely found in high enough concentrations to make economically viable deposits (Long et al., 2010). Currently, China controls >90% of the world's supply of REEs (Chen, 2011), presenting the potential for a supply problem. Understanding basic material properties of REE bearing minerals such as the temperatures at which different phases are thermodynamically stable and how they respond to changes in temperature can assist in understanding how economically viable deposits might form, thereby potentially leading to the discovery of new deposits.

Having the general formula of $(Ce,La,Nd,Y)CO_3(F,OH)$, bastnaesite is the most common mineral mined for REEs. It occurs mainly in carbonatites and is usually found in association with calcite, dolomite, and barite. Bastnaesite-(La) is the lanthanum fluoride end member ($LaCO_3F$) (Oftedal, 1931; Donnay and Donnay, 1953; Ni et al., 1993; Long et al., 2010; Castor, 2008a, 2008b). This work explores the ambient pressure thermal behavior of bastnaesite-(La) and the oxyfluorides it decomposes to using thermogravimetric analysis, differential scanning calorimetry, and heated X-ray powder diffraction.

Background

Structure and decomposition of bastnaesite-(La) to lanthanum oxyfluoride

Bastnaesite-(La) ($LaCO_3F$) exhibits hexagonal symmetry in the P-62c space group. Each unit cell contains six formula units of alternating layers of carbonate anions and layers of lanthanum cations and fluorine anions. The lanthanum-fluoride layers are parallel to the *a*- axis while the carbonate anion groups between them are locally parallel to the *c*- axis (Donnay and Donnay, 1953; Oftedal, 1931; Ni et al., 1993). A structural model is shown in figure 2-1 (Momma and Izumi, 2011). With the application of sufficient heat, bastnaesite-(La) decomposes via the decarbonation reaction $LaCO_3F$ + (heat) = LaOF + CO_2. At ambient conditions, γ-LaOF exhibits tetragonal symmetry in the P4/nmm space group with two formula units per unit cell (Woo et al., 2013; Jacob et al., 2006; Fergus and Chen, 2000; Shinn and Eick, 1969; Zachariasen, 1951). A structural model of γ-LaOF is shown in figure 2-2 (Momma and Izumi, 2011). At high temperature, α-LaOF is stable with cubic symmetry in the Fm-3m space group with four formula units per unit cell (Pistorius, 1973; Klemm and Klein, 1941; Mathews et al., 1997; Achary et al., 1998; Holtstam et al., 2004). A structural model of α-LaOF is shown in figure 2-3 (Momma and Izumi, 2011). β-LaOF is reported as stable at ambient pressure and temperature exhibiting rhombohedral symmetry in the R-3m space group with six formula units per unit cell (Achary et al., 1998; Woo et al., 2013; Zachariasen, 1951). This structure was not encountered during this investigation.

Thermal expansion coefficient

The change in volume of a material due to changes in thermodynamic state variables, such as temperature or pressure, changes the free energy of the material, which determines whether the

material is stable. Thermal expansion describes the change of volume or length of a material with respect to changes in temperature, and is defined in terms of the thermal expansion coefficient:

$$\alpha = \frac{1}{V}\left(\frac{\partial V}{\partial T}\right)_P$$

where α is the coefficient, V is the volume, and T is the temperature. For crystalline materials over large ranges of temperature, the change in thermal expansion is not linear, but for measurements over limited ranges of temperatures, it can be described by the polynomial:

$$\alpha(T) = a_0 + a_1 T + a_2 T^{-2}$$

where α is the mean thermal expansion coefficient, T is the measured temperature and a_0, a_1 and a_2 are constants fit from experimental data. For most solids at ambient pressure, the thermal equation of state:

$$V(T) = V_0 \times e^{\left[a_0(T-298)+\frac{1}{2}a_1(T-298)^2+a_2\left(\frac{1}{T}-\frac{1}{298}\right)\right]}$$

allows the calculation of the high temperature volume at ambient pressure, where V_0 is the volume at a reference temperature (298 K) and T is the measured temperature (Fei, 1995).

Methods

Synthesis

Bastnaesite-(La) was synthesized via precipitation from an aqueous solution at room pressure and temperature using the method described by Janka and Schleid (2009). Aqueous solutions of each reagent were made by mixing powdered lanthanum nitrate ($La(NO_3)_3 \cdot 6H_2O$,

Sigma Aldrich 203548-100G, >99% purity), sodium bicarbonate ($NaHCO_3$, Sigma Aldrich S6014-25G, >99% purity), and sodium fluoride (NaF, Sigma Aldrich 201154-5G, >99% purity) with deionized water in separate beakers. The solutions were combined in a larger beaker. Bastnaesite-(La) precipitated from the solution immediately, with sodium nitrate ($NaNO_3$) remaining in solution. The fluid was decanted, and the bastnaesite-(La) precipitate was washed in deionized water and then centrifuged to remove any residual sodium nitrate. The powder was then dried in a Fischer Scientific model 289A Isotemp Vacuum oven under vacuum at 215°C (488 K) for at least 12 hours.

Phase identification was completed by powder X-ray diffraction in a PANalytical X'Pert PRO and photoaccoustic infrared spectroscopy on a Digilab FTS-7000 Fourier transfer infrared (FTIR) spectrometer. Rietveld structure refinement using X'pert Highscore Plus software was used to determine that the bastnaesite-(La) starting material contained <10% LaF_3 impurity. No OH peaks were detected by FTIR between 3600 and 3400 cm^{-1}.

The powder X-ray diffraction peaks from the synthesized bastnaesite-(La) are wide due to the small particle size, so the material was next annealed in a Griggs modified piston cylinder apparatus (Tullis and Tullis, 1986) using NaCl as the pressure transmitting medium. Samples were placed in a platinum jacket, surrounded by graphite, and sealed in a copper capsule then subjected to pressures between 0.25 and 1.0 GPa and temperatures from 700°C to 900°C. See figure 2-4 for comparison of diffraction patterns before and after annealing.

Themogravimetric analysis and differential scanning calorimetry

Thermogravimetric analysis (TGA) was used to determine the temperature at which bastnaesite-(La) begins to decompose, and differential scanning calorimetry (DSC) was used to

determine the temperatures of any other first order phase transformations. Powdered samples of at least 5mg were heated in an alumina crucible in a Netzsch STA449 F1 Jupiter DSC/TGA apparatus under dry N_2 at 1 atm pressure at a programmed rate of 5°/min from 313 K to 1223 K. A second empty alumina crucible was used as the reference. A Pfeiffer Vacuum Thermostar Quadrupole mass spectrometer was used to detect CO_2 from the decomposition of bastnaesite-(La).

During an experimental run, thermogravimetric analysis and differential scanning calorimetry each produce data that create a curve that describes the sample's response to the applied heat energy. Figure 2-5 contains TGA curves used in this study. During a TGA run, the curve is recorded in terms of mass remaining on the y-axis and elapsed time or measured temperature on the x-axis, beginning with 100% mass at time=0 or initial temperature. The atmosphere in the experimental apparatus should be carefully controlled so that it will not react with the sample. Ideally, a curve should always have a flat or negative slope because the mass of the sample can only remain constant or decrease. Since even the most carefully prepared samples likely contain water, most experimental run curves exhibit a small and constant loss of mass from the very start that is interpreted as surface water dehydrating. At any temperature that a volatizing reaction occurs, the slope steepens until the reaction completes. Any change in slope will signal either the initiation or completion of a reaction; the steepness of the slope relates to the kinetics of the reaction.

Figure 2-6 contains DSC curves used in this study. During a DSC run, the data collected produce a curve that reports the difference in energy or heat flow required to maintain the rate of temperature increase in the sample relative to the reference crucible on the y-axis and elapsed time or measured temperature on the x-axis. An "endotherm" occurs when the curve's slope changes sharply or discontinuously upwards; the behavior of the curve is due to the sample requiring an

increase in energy to maintain the same rate of temperature increase as the reference crucible, and is interpreted as the sample undergoing an endothermic reaction. An "exotherm" occurs when the curve's slope changes sharply or discontinuously downwards; the behavior of the curve is due to the sample requiring a decrease in energy to maintain the same rate of temperature increase as the reference crucible, and is interpreted as the sample experiencing an exothermic reaction. Gentle changes in slope of the curve can be attributed to imperfect insulation leading to heat loss to the outside environment, errors in measurement, or changes in the heat capacity of the sample material (Sarge et al., 2014).

Heated powder X-ray diffraction

Heated powder X-ray diffraction was used to determine unit cell volume as a function of temperature and to determine which structures were present at those temperatures. Measurements were made in air on a PANalytical X'Pert Pro MPD Diffractometer fitted with an Anton Paar XRK 900 thermal reactor stage and an X'celerator (2.02° 2θ) detector. A cobalt X-ray source (Co $K\alpha_1$ λ=1.78901 Å) was used in angular dispersive mode from 4.098 to 79.9814 °2θ with a step size of 0.0170° at 50.1650 seconds per step. Diffraction patterns were collected at 298 K, and in 50 degree increments from 323 K to 473 K, and in 25 degree increments from 473 K to 1173 K. A final pattern was collected at 298 K after the sample was allowed to cool. Data analysis was completed using QualX 2.0 (Altomare et al., 2015), UnitCellWin64 (Holland and Redfern, 1997) and EosFit7GUI (Angel et al., 2014).

Results

Thermogravimetric analysis and differential scanning calorimetry

Thermogravimetric analysis and mass spectrometry CO_2 detection curves for annealed bastnaesite-(La), unannealed starting material, and LaOF are displayed in figure 2-5. At the beginning of the thermal analysis for samples containing bastnaesite-(La), from 313 K to 600 K, a small amount of mass loss is interpreted to be loss of surface water adsorbed onto the sample material. Above this temperature, the curve for mass loss steepens as the decomposition reaction of bastnaesite-(La) to γ-LaOF begins. Differential scanning calorimetry curves for annealed bastnaesite-(La), unannealed starting material, and LaOF are displayed in figure 2-6. The DSC curve also steepens in this range, exhibiting an exotherm, and the mass spectrometer begins to detect CO_2. The exothem and mass loss continue on both curves until 773 K, where the detection of CO_2 also peaks. All three samples exhibit endotherms at 948 K and 1123 K, indicative of phase transitions.

Heated powder X-ray diffraction

Figure 2-7 displays all heated powder X-ray diffraction patterns in this study, and figure 2-8 displays the heated powder XRD patterns encompassing the bastnaesite-(La) decomposition reaction. Bastnaesite-(La) is the dominant species in the X-ray diffraction patterns from 298 K to 723 K. Diffraction peaks for γ-LaOF begin to show up in the patterns above 598 K. By 773 K, bastnaesite-(La) is no longer present in the patterns, and γ-LaOF is the only phase present. Above 948 K, only α-LaOF is present. γ-LaOF was the only species present in the pattern collected at 298 K after the sample was allowed to cool down following the collection of the final high temperature pattern. β-LaOF was not evident in any of patterns. See tables 2-1 to 2-3 for the measured lattice

parameters and volumes of all three materials. Figures 2-9, 2-10, and 2-11 display measured unit cell volumes as a function of temperature for all three materials.

Discussion and conclusions

From TGA/DSC and heated powder XRD data, it is apparent that at ambient pressure, bastnaesite-(La) is stable until 598 K. Above this temperature, the decomposition reaction of bastnaesite-(La) into γ-LaOF and CO_2 begins, but proceeds slowly. As expected, an increase in the temperature results in an increase in the reaction rate. At 948 K, tetragonal γ-LaOF undergoes a first order structural phase transition reaction to cubic α-LaOF. The decomposition temperature for bastnaesite-(La) found in this study agrees with previous values reported by Janka and Schlied (2009) who used similar methods, but they did not report behavior for temperatures above 823 K. While the sample material cooled back down to 298 K, it transformed to γ-LaOF, the stable structure of LaOF at ambient conditions. The bastnaesite-(La) decomposition reaction to LaOF and CO_2 could not reverse because the CO_2 left the sample during the experiment.

Table 2-4 lists the fitted thermal expansion coefficients for bastnaesite-(La), γ-LaOF, and α-LaOF over the temperature ranges that unit cells were measured in the heated powder X-ray diffraction experiments. Over the temperature ranges measured, all three species exhibit a trend of positive linear thermal expansion as temperatures are increased. Figures 2-9, 2-10, and 2-11 illustrate this behavior. At the highest temperatures measured, 1123 K and 1173 K, the data indicate that α-LaOF unit cell volume reverses this trend and begins to contract. There is an endotherm in the DSC curve at 1123 K which could indicate a phase transition, but the X-ray diffraction patterns at these temperatures do not indicate a different structure, so further studies are necessary to determine what this endotherm represents.

Thermal analysis has not been performed on any other fluorocarbonate minerals, so a direct comparison of the properties of bastnaesite-(La) measured in this investigation to other materials with similar structure is not possible. Others have investigated the thermal expansion of more common carbonates including aragonite ($CaCO_3$), strontianite ($SrCO_3$), cerrusite ($PbCO_3$), witherite ($BaCO_3$) (Ye et al., 2012), calcite ($CaCO_3$), and magnesite ($MgCO_3$) (Markgraf and Reeder, 1985). A comparison of the thermal equations of state for bastnaesite-(La) and these materials is illustrated in figure 2-12. Compared with these more common carbonates, bastnaesite-(La) experiences more thermal expansion for a given increase in temperature than the trigonal R-3c carbonates (calcite and magnesite), and less thermal expansion for a given increase in temperature than the orthorhombic Pmcn carbonates (aragonite, cerrusite, strontianite, and witherite). Also of note, as described in table 2-4, bastnaesite-(La)'s *a*- and *c*- crystallographic axes expand at different rates; all of the other carbonates listed above also exhibit some degree of anisotropic thermal expansion. Overall, this indicates that bastnaesite-(La)'s thermal expansion behavior is similar to that of other carbonate minerals.

There are no previous studies of tetragonal REE-bearing oxyfluorides, but Achary et. al (1998) reported the synthesis of the rhombohedral oxyfluoride of five REE's (La, Nd, Sm, Eu, and Gd), and used heated powder XRD to investigate the thermal expansion and phase transformation to cubic structures at high temperature. Their calculation and fitting of thermal expansion coefficients used the data for both rhombohedral and cubic phases, so the resulting thermal equations of state are not suitable to compare directly to those for α-LaOF in this study. Using their data for the cubic phases, thermal expansion coefficients were fit in EOSFit7GUI (Angel et al., 2014). Table 5 lists the fitted coefficients, and figure 2-13 illustrates the thermal equations of state compared to that of α-LaOF measured in this study. The thermal expansion behavior we

measured for α-LaOF is very similar to their findings, and most of the REE-bearing oxyfluorides follow a trend of the ultimate unit cell volume being a function of the REE ion size; if measurements of CeOF and PrOF were available, we could safely hypothesize that they would plot between LaOF and NdOF.

There are some differences in our results compared to those of as Achary et al. (1998). Those authors started with rhombohedral oxyfluorides, and found the transition from rhombohedral to cubic occurs at a lower temperature (between 703 and 823 K) than we found for the tetragonal to cubic transition. In their synthesis methods, they found that a small excess of fluorine stabilized the tetragonal phase in place of the rhombohedral phase. Our synthesis products did contain a small amount of LaF_3 and we were unable to synthesize the rhombohedral phase of LaOF. They reported being unable to locate the tetragonal to rhombohedral phase transitions, but did not report what temperature range was investigated. It is possible that the small excess of fluorine in our starting material is also the cause of the small but measurable increase in unit cell volume at high temperature over theirs. Since geologic processes are unlikely to be perfectly stoichiometric, our results could be typical of a fluorine enriched system while theirs could be typical of a fluorine depleted system.

Tables

Temperature (K)	*a* (Å)	Uncertainty	*c* (Å)	Uncertainty	V (Å^3)	Uncertainty
298	7.1867	0.00085	9.8328	0.00083	439.82	0.185
323	7.1897	0.00085	9.8347	0.00083	440.26	0.185
373	7.1954	0.00085	9.8394	0.00083	441.18	0.185
423	7.1992	0.00085	9.8438	0.00083	441.84	0.185
473	7.2044	0.00085	9.8486	0.00083	442.69	0.186
498	7.2074	0.00085	9.8504	0.00083	443.14	0.186
523	7.2096	0.00085	9.8539	0.00083	443.57	0.186
548	7.2125	0.00085	9.8564	0.00083	444.04	0.186
573	7.2159	0.00085	9.8572	0.00083	444.50	0.186
598	7.2172	0.00085	9.8598	0.00083	444.76	0.186
623	7.2205	0.00086	9.8626	0.00083	445.30	0.186
648	7.2238	0.00086	9.8669	0.00083	445.91	0.187
673	7.2266	0.00086	9.8669	0.00083	446.25	0.187
698	7.2296	0.00086	9.8730	0.00083	446.90	0.187
723	7.2339	0.00086	9.8731	0.00083	447.43	0.187

Table 2-1: Measured lattice parameters and volume for bastnaesite-(La) from 298 K to 723 K.

Temperature (K)	*a* (Å)	Uncertainty	*c* (Å)	Uncertainty	V (Å^3)	Uncertainty
298	4.0798	0.00041	5.798	0.0020	96.51	0.118
723	4.1242	0.00045	5.855	0.0030	99.59	0.130
748	4.1192	0.00041	5.873	0.0020	99.65	0.119
773	4.1192	0.00041	5.873	0.0020	99.65	0.119
798	4.1213	0.00042	5.862	0.0020	99.57	0.119
823	4.1230	0.00042	5.862	0.0020	99.64	0.119
848	4.1246	0.00042	5.867	0.0020	99.80	0.119
873	4.1276	0.00042	5.864	0.0020	99.91	0.119
898	4.1293	0.00042	5.860	0.0020	99.92	0.119
923	4.1286	0.00050	5.866	0.0022	99.99	0.122
948	4.1311	0.00042	5.859	0.0020	100.00	0.119

Table 2-2: Measured lattice parameters and volumes for γ-LaOF at 298 K, and from 723 K to 948 K.

Temperature (K)	*a* (Å)	Uncertainty	V (Å^3)	Uncertainty
298	5.756*	0.003*	190.71*	
973	5.8424	0.00049	199.42	0.138
998	5.8443	0.00049	199.62	0.138
1023	5.8476	0.00050	199.95	0.138
1048	5.8489	0.00050	200.08	0.138
1073	5.8500	0.00050	200.20	0.138
1098	5.8526	0.00050	200.47	0.138
1123	5.8538	0.00050	200.60	0.138
1148	5.8531	0.00050	200.52	0.138
1173	5.8511	0.00050	200.32	0.138

*Table 2-3: Measured lattice parameters and volumes for α-LaOF from 973 K to 1173 K. *values for ambient temperature (298 K) from* (Klemm and Klein, 1941) *because this structure was not recoverable to room temperature by quenching in the XRK-900 reactor stage.*

Material		Temp. Range (K)	α_{298}	a_0	a_1	a_2
bastnaesite-(La)	*a*(a_0=7.1867 Å)	298-723	0.0000173	-0.0000108	0.0000000373	1.502
	c(c_0=9.8328 Å)	298-723	0.00000951	0.00000247	0.0000000116	0.319
	V(V_0=439.82 Å^3)	298-723	0.0000432	-0.0000168	0.0000000834	3.126
γ-LaOF	*a*(a_0=4.0798 Å)	723-948	0.000135	-0.000179	0.000000190	22.879
	c(c_0=5.798 Å)	723-948	0.00000179	0.000001785	-0.0000000229	8.154
	V(V_0=96.51 Å^3)	723-948	0.000295	-0.000241	0.000000242	41.147
α-LaOF	*a*(a_0=5.756 Å)	973-1123	-0.00000844	0.0000846	-0.0000000625	-6.606
	V(V_0=190.71 Å^3)	973-1123	-0.0000112	0.000236	-0.000000173	-17.362

Table 2-4: Calculated thermal expansion coefficients for bastnaesite-(La), γ-LaOF, and α-LaOF along crystallographic axes and for volume. Reference temperature for all fits is 298 K.

Material	Temp. Range (K)	V_o (Å^3)	α_{298}	a_o	a_1	a_2
α-LaOF (this study)	973-1123	190.71	-0.0000112	0.000236	-0.000000173	-17.362
α-LaOF (from Achary)	823-1077	196.1	0.00000855	0.000000017	0.0000000286	0.0001
NdOF (from Achary)	823-1075	183.8	0.00000268	0.000000007	0.00000000895	0.0001
SmOF (from Achary)	811-1075	176.2	0.000014	0.000014	0.000000000028	0
EuOF (from Achary)	815-1077	168.2	0.0000449	0.0000449	0.000000000052	0.0001
GdOF (from Achary)	913-1067	172.6	0.00000461	0.000000044	0.00000001530	0

Table 2-5: Calculated thermal expansion coefficients for cubic REE-oxyfuorides. α-LaOF measured in this study is compared to data from Achary, et. al (1998). Reference temperature for all fits is 298 K.

Figures

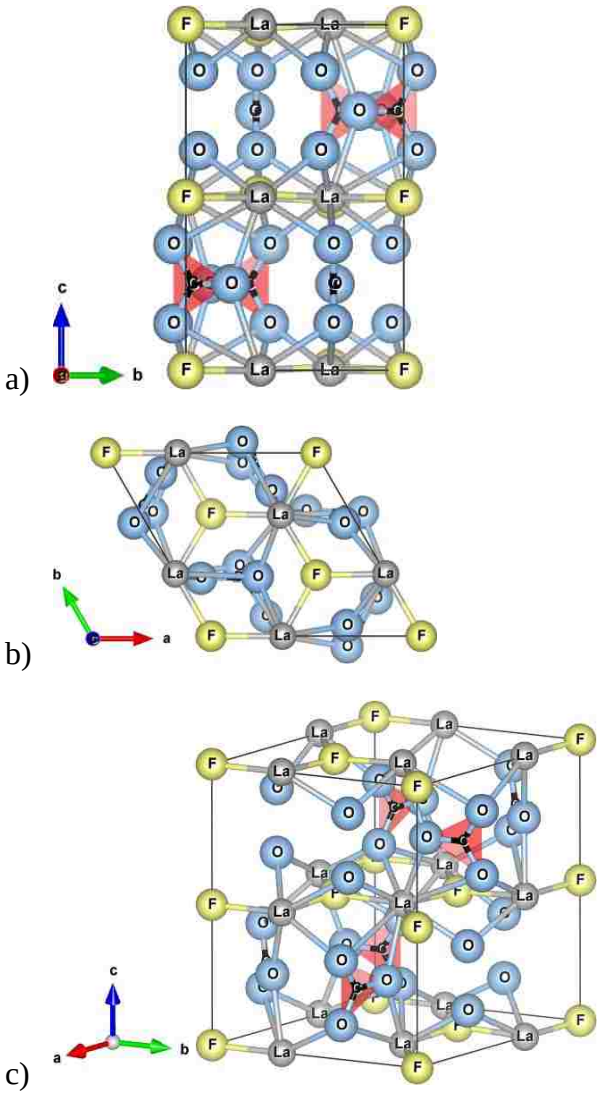

Figure 2-1: Structure of bastnaesite-(La) generated in the software VESTA (Momma and Izumi, 2011)*, a) as viewed down the a- axis, b) as viewed down the c- axis, and c) as viewed from an arbitrary angle* (Ni et al., 1993).

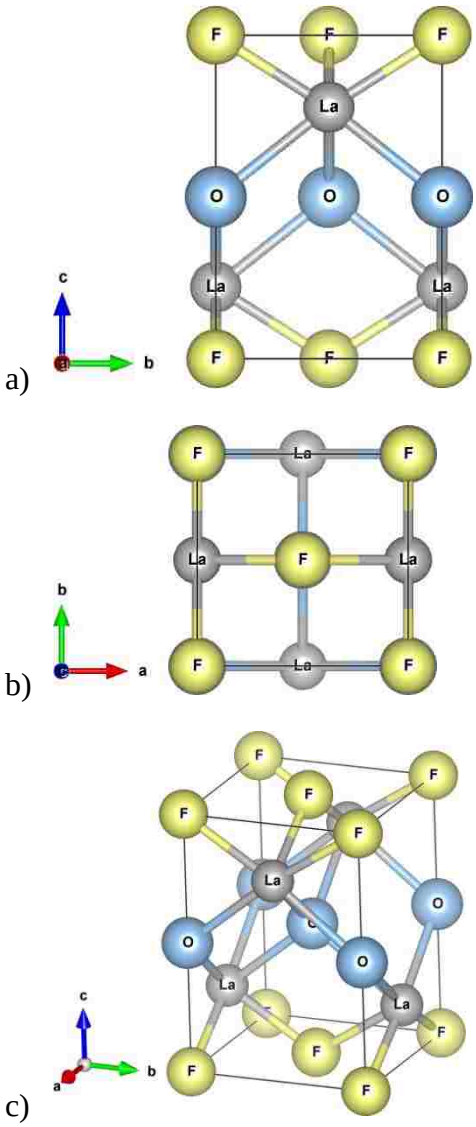

Figure 2-2: Structure of tetragonal γ-LaOF generated in the software VESTA (Momma and Izumi, 2011) *a) as viewed down the a- axis, b) as viewed down the c- axis, and c) as viewed from an arbitrary angle* (Zachariasen, 1951).

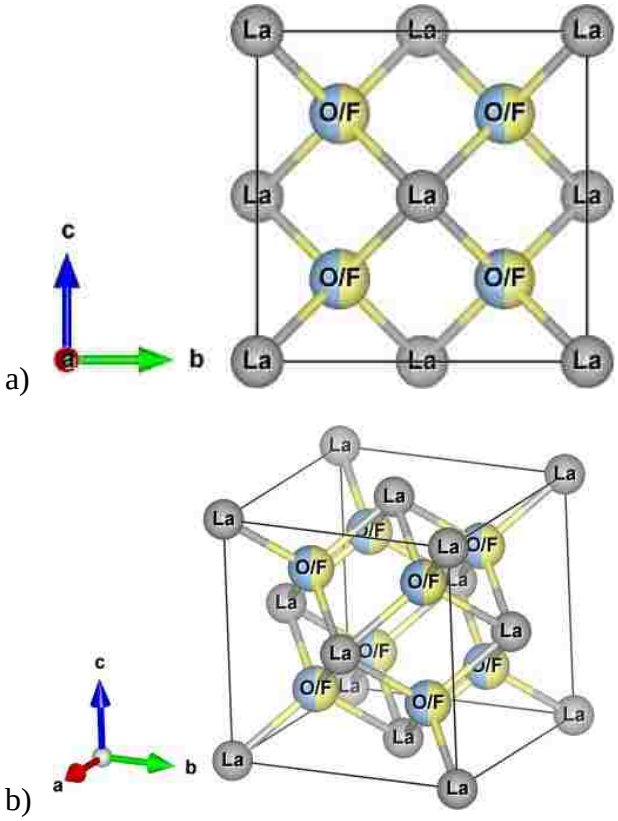

Figure 2-3: Structure of cubic α-LaOF generated in the software VESTA (Momma and Izumi, 2011) *a) as viewed down the a- axis, and b) as viewed from an arbitrary angle* (Holtstam et al., 2004).

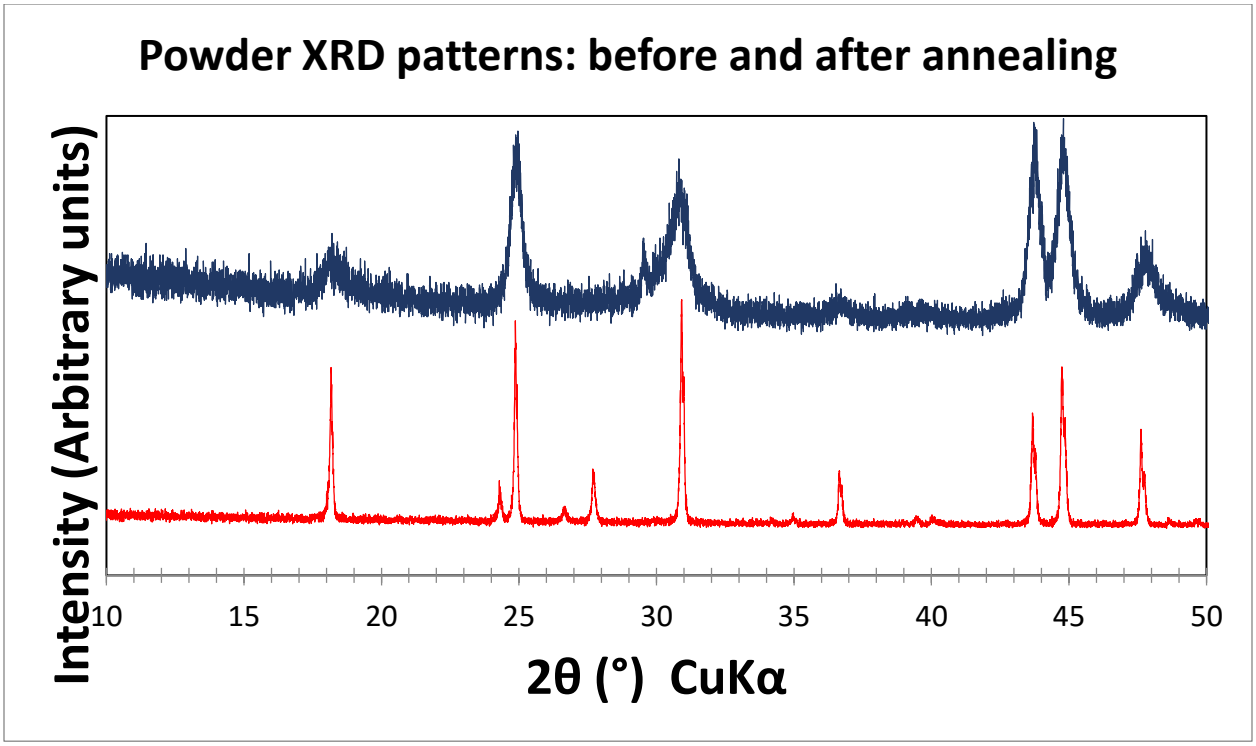

Figure 2-4: Powder XRD patterns of synthesized bastnaesite-(La) starting material. Top pattern is after washing and drying, bottom pattern is after annealing in the Griggs modified piston cylinder apparatus.

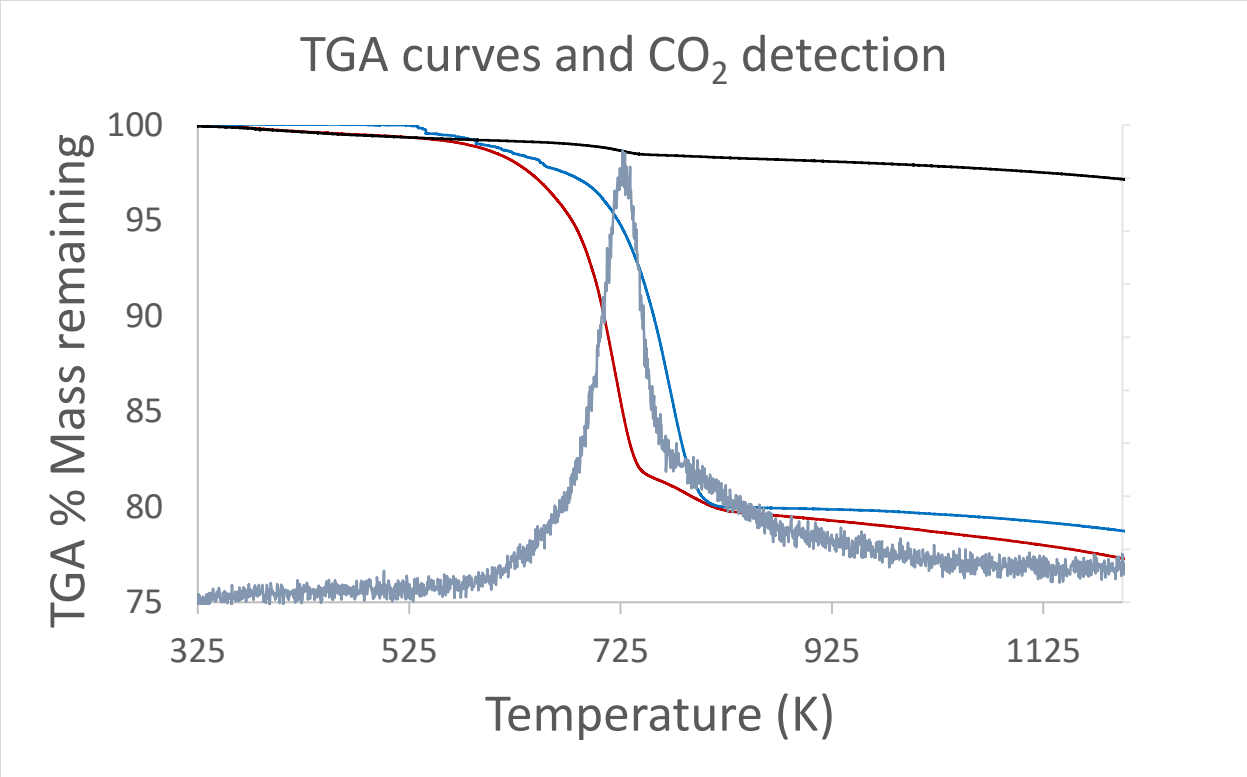

Figure 2-5: Thermogravimetric analysis curves for (blue) annealed bastnaesite-(La), (red) un-annealed starting material, and (black) LaOF from 325 K to 1223 K. CO_2 detection from the Pfeiffer Vacuum Thermostar Quadrupole mass spectrometer in light gray. Mass loss curves for the starting material and annealed bastnaesite-(La) begin to steepen at 600 K, at the same time CO_2 detection begins. The mass loss curve for LaOF does not steepen then, as the decomposition reaction did not occur in that sample.

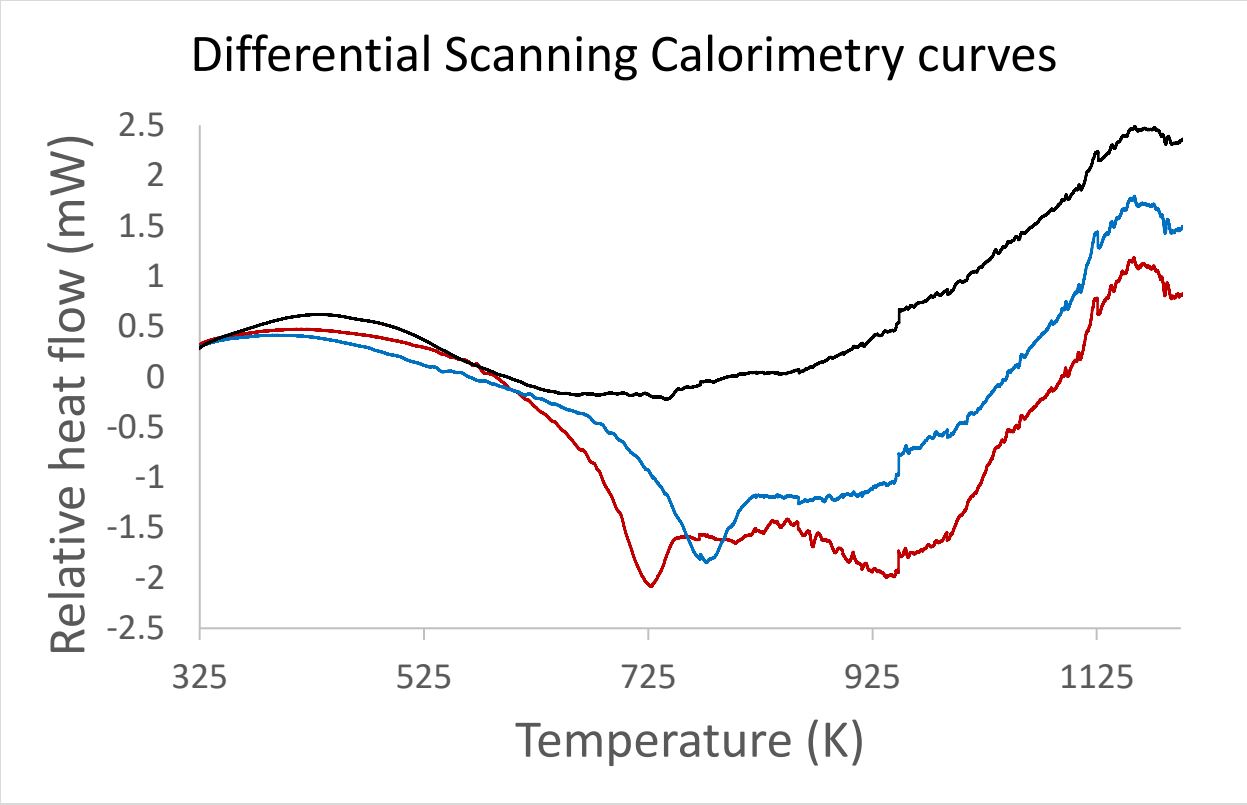

Figure 2-6: Differential scanning calorimetry curves for (blue) annealed bastnaesite-(La), (red) un-annealed starting material, and (black) LaOF from 325 to 1223 K. Exotherms can be seen on both the annealed bastnaesite-(La) and un-annealed starting material curves from the range near 598 K to 773 K indicating the decomposition reaction. The LaOF curve does not exhibit this, since it did not decompose. Endotherms are evident on all three curves at 948 K and 1123 K indicating phase transformations.

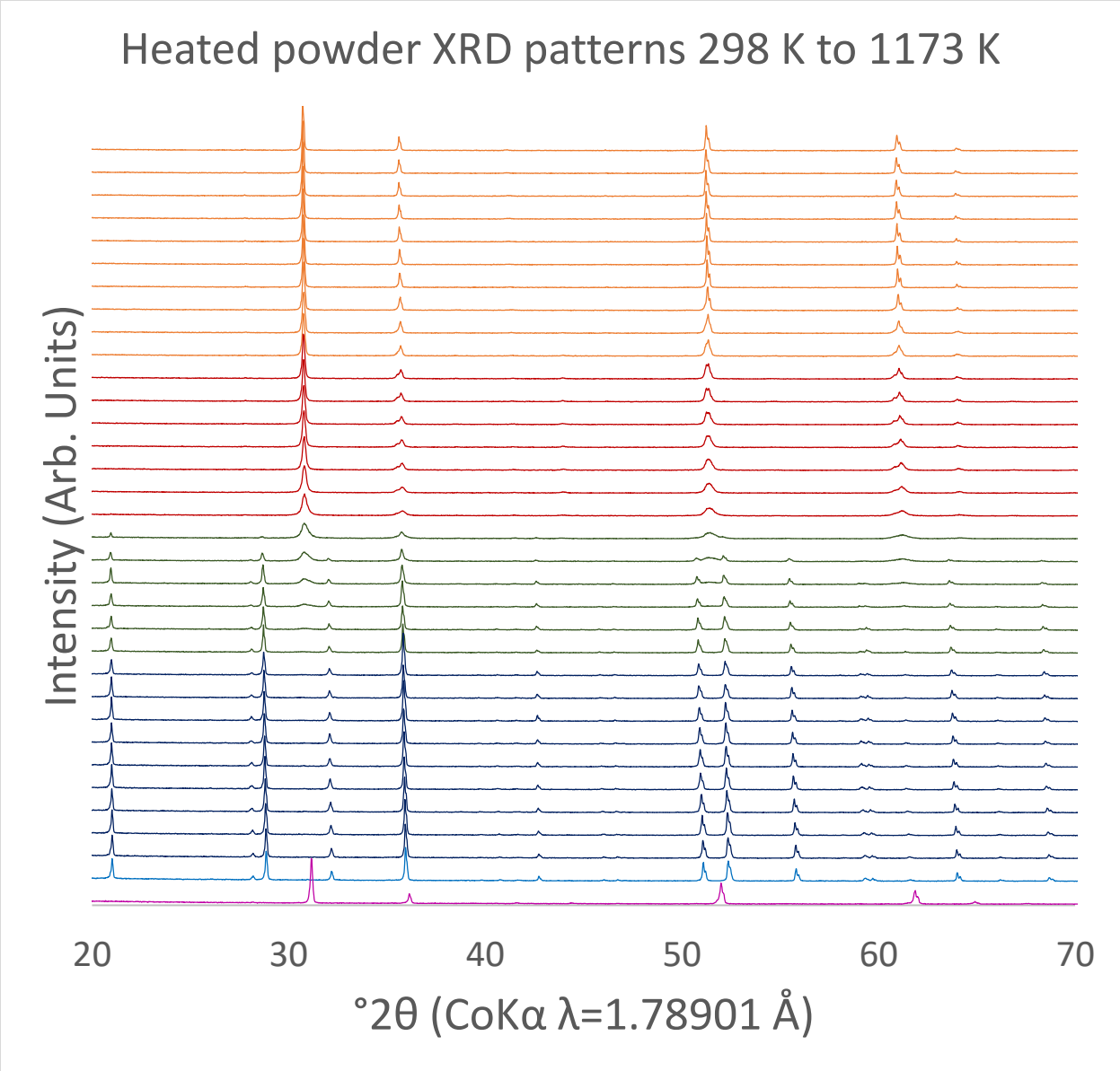

Figure 2-7: Heated powder X-ray diffraction patterns from 298 K to 1173 K. Two 298 K patterns are at the bottom, and temperatures increase upward in 50 degree increments from 323 K to 473 K. and then in 25 degree increments from 473 K to 1173 K. Bottom most pattern is the 298 K pattern collected after the sample was allowed to cool, and is representative of γ-LaOF. Bastnaesite-(La) is the dominant feature of patterns from 298 K to 723 K. γ-LaOF begins to show up above 600 K, and is the only species in the patterns from 773 K to 948 K. Above 948 K, only α-LaOF is present in the patterns.

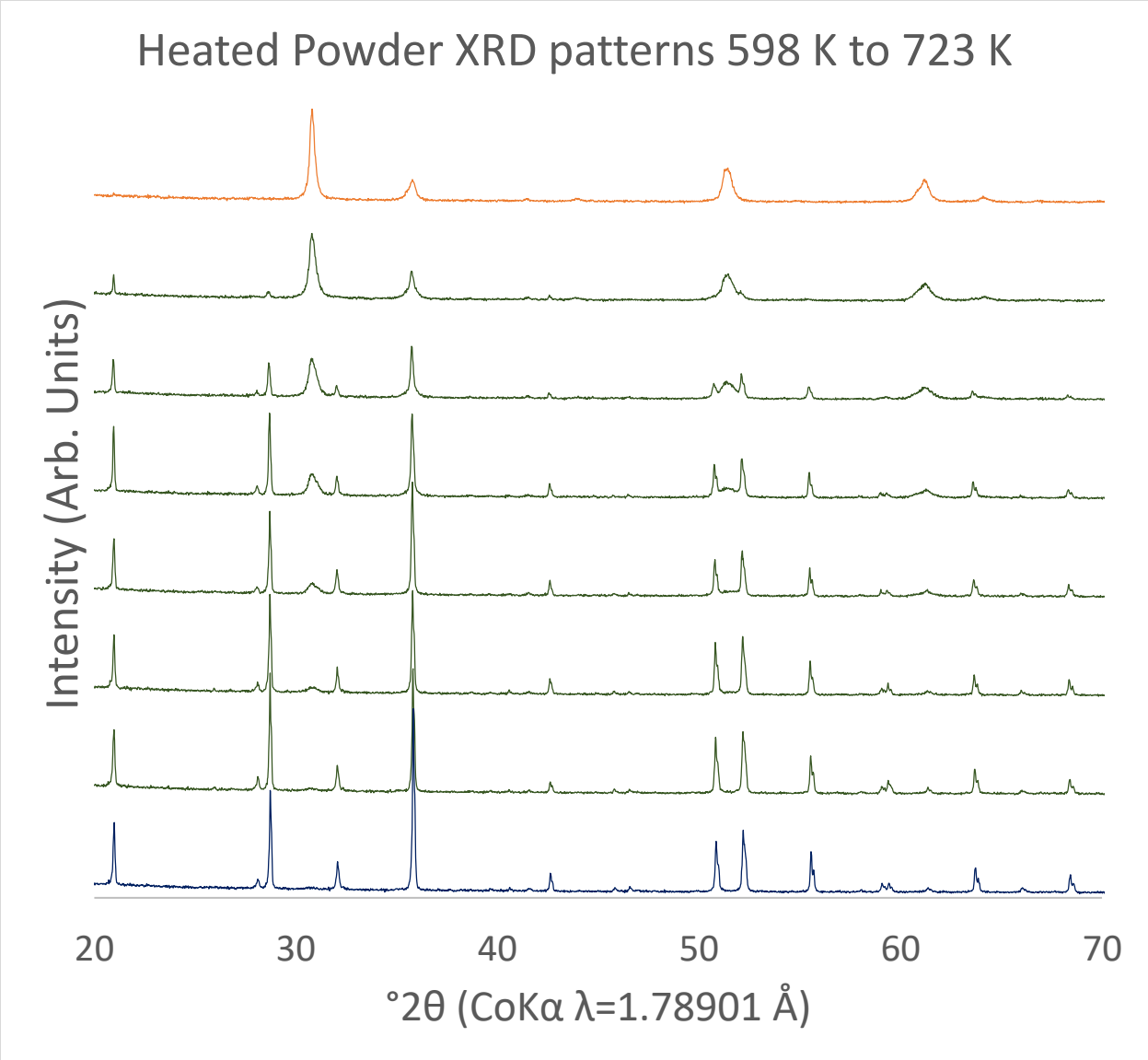

Figure 2-8: Heated powder X-ray diffraction patterns from 598 K to 723 K. Bottom pattern is 598 K, and the patterns go up in 25°temperature increments. Bottom most pattern exhibits bastnaesite-(La) and no γ-LaOF. Top most pattern exhibits only γ-LaOF. The middle 6 patterns exhibit both species as the decomposition reaction progresses from bastnaesite-(La) to γ-LaOF.

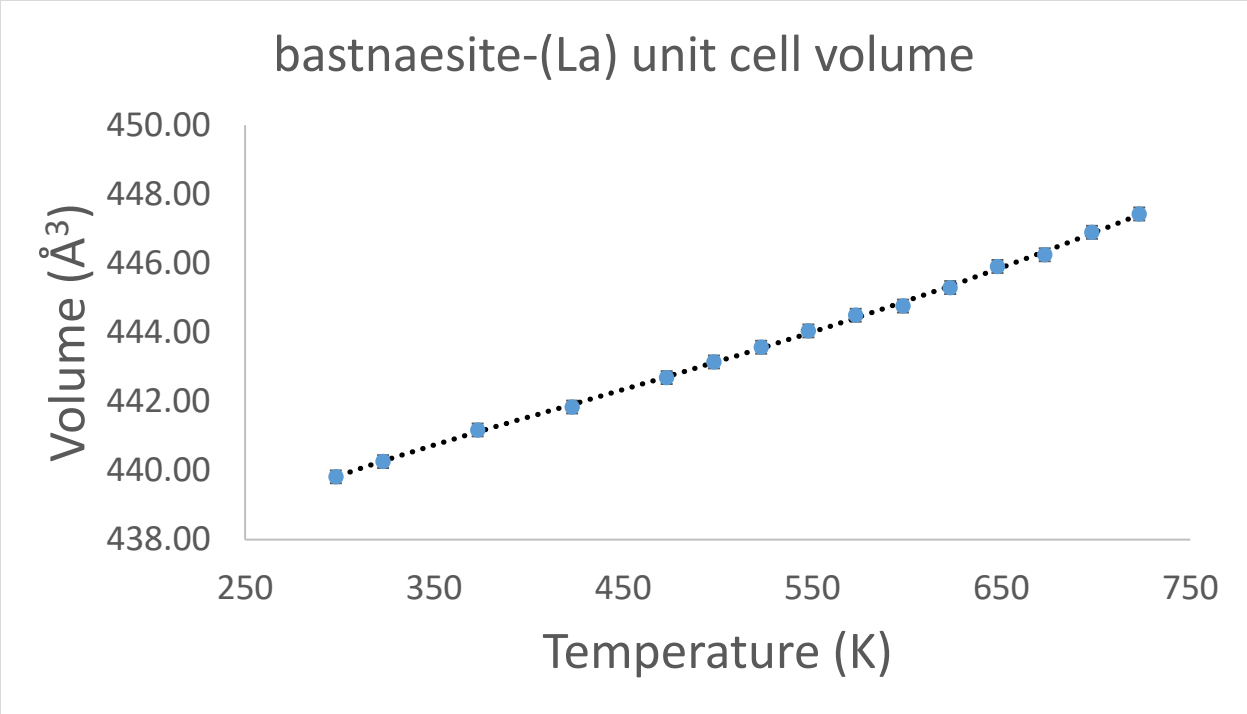

Figure 2-9: Measured unit cell volumes for bastnaesite-(La) as a function of temperature from 298 K to 723 K. The dotted black line is the fit for the Fei thermal equation of state (Fei, 1995).

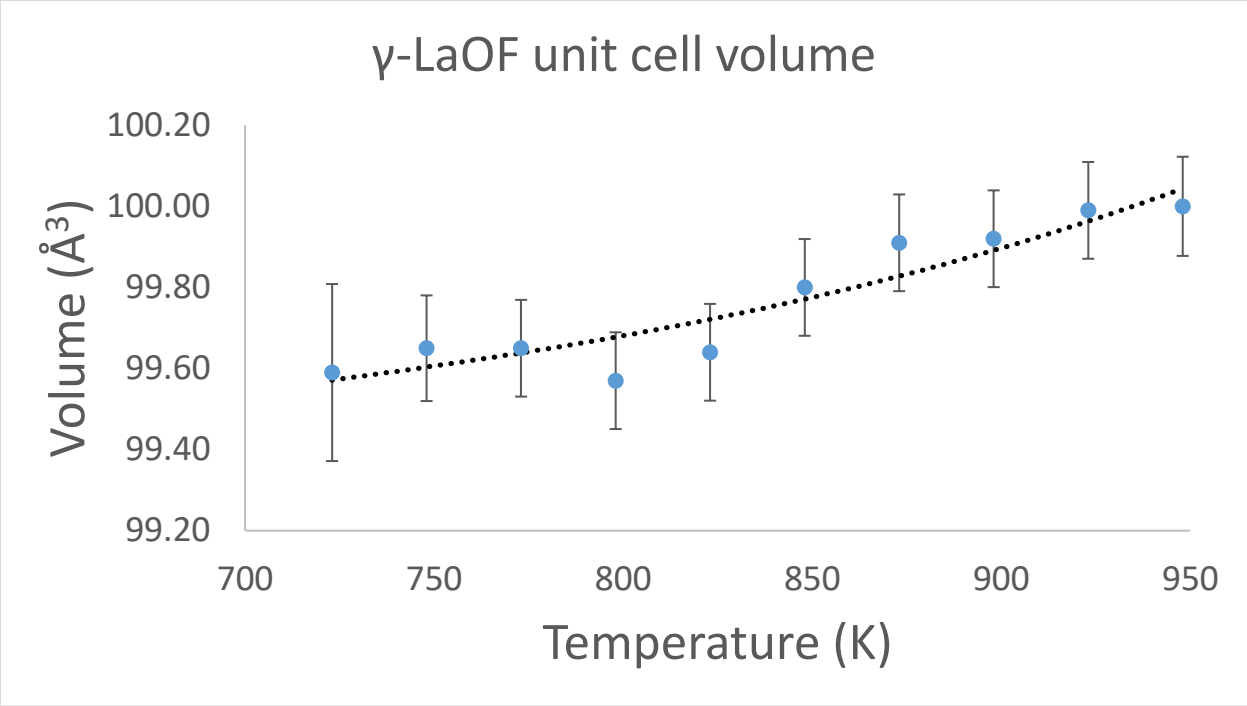

Figure 2-10:Measured unit cell volumes for tetragonal γ-LaOF as a function of temperature from 723 K to 948 K. The dotted black line is the fit for the Fei thermal equation of state (Fei, 1995).

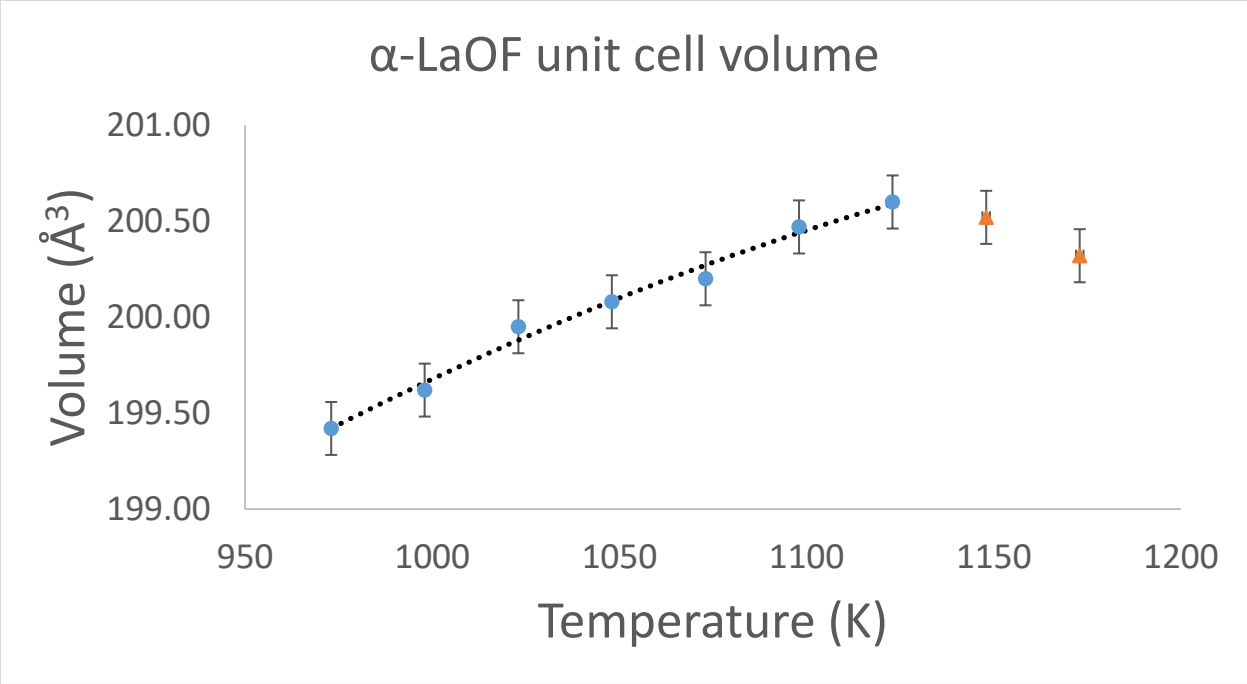

Figure 2-11: Measured unit cell volumes for cubic α-LaOF as a function of temperature from 973 K to 1123 K. Blue circles represent data used to fit the thermal equation of state in this temperature range. Orange triangles represent temperature points 1148 and 1173 which are above the temperature that coincides with a contraction in unit cell volume and an endotherm on the DSC curve. The dotted black line is the fit for the Fei thermal equation of state (Fei, 1995).

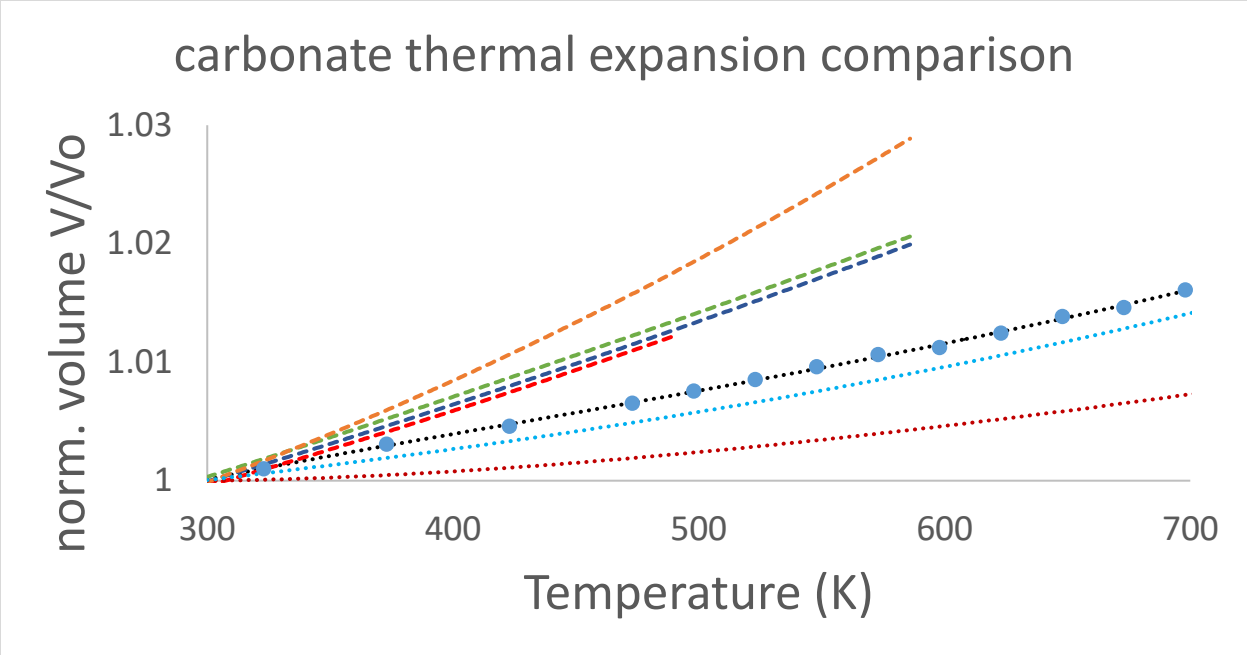

Figure 2-12: Comparisons of ambient pressure thermal equations of state for different carbonate minerals. Blue circles represent bastnaesite-(La) data from this study, and the dotted black line represent the fitted Fei equation of state (Fei, 1995) *for bastnaesite-(La). Thermal equations of state are shown for calcite ($CaCO_3$, red dotted line), magnesite ($MgCO_3$, blue dotted line)* (Markgraf and Reeder, 1985), *witherite ($BaCO_3$, red dashed line), cerrusite ($PbCO_3$, orange dashed line), strontianite ($SrCO_3$, green dashed line), and aragonite ($CaCO_3$, blue dashed line)* (Ye et al., 2012).

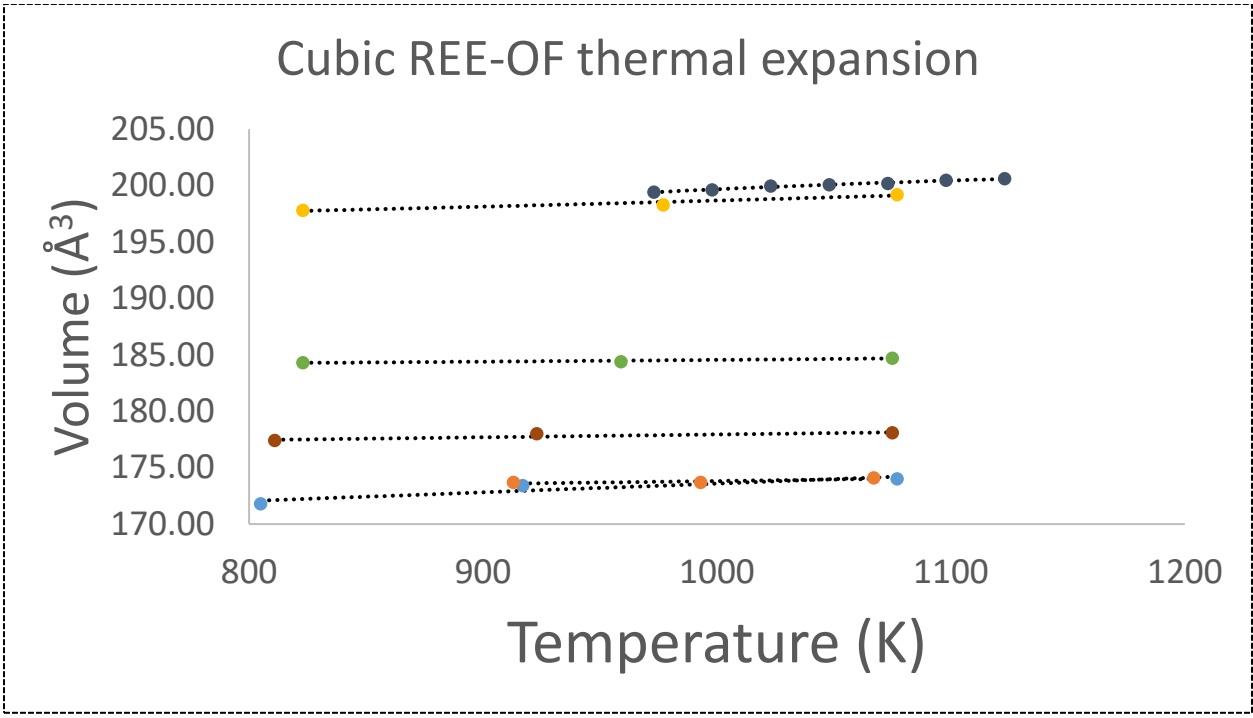

Figure 2-13:Comparisons of ambient pressure thermal equations of state for cubic REE-OF compounds from this study and using data from Achary et al. (1998). Gray circles are data for cubic α-LaOF from this study. Yellow circles are data for cubic α-LaOF, green circles are data for cubic NdOF, red circles are data for cubic SmOF, blue circles are data for cubic EuOF, and orange circles are data for cubic GdOF from (Achary et al., 1998)

Chapter 3 – Compressibility of bastnaesite-(La)

Abstract

Understanding basic material properties of rare earth element (REE)-bearing minerals such as the pressures at which different phases are thermodynamically stable and how they respond to changes in pressure or temperature can assist in understanding how economically viable deposits might form, thereby potentially leading to the discovery of new deposits. Bastnaesite is the most common REE-bearing mineral mined. The lanthanum-rich end member, bastnaesite-(La), was synthesized and its thermodynamic behavior from ambient pressure to 11.3 GPa at ambient temperature and from 4.9 to 7.7 GPa up to 400°C was investigated through in-situ single crystal X-ray diffraction in diamond anvil cells. At ambient temperature, a 3rd-order Birch-Murnaghan equation of state was fit for bastnaesite-(La) with V_o = 439.82 Å^3, K_o = 105 GPa, and K' =5.58.

Introduction

The rare earth elements (REE), also known as the lanthanides, are the first on the periodic table to begin populating f-block orbitals and thus exhibit unique electronic properties. Because of this, they are sought after for various technological applications for which other metals are not suitable. Relative crustal abundances of REEs are higher than noble metals such as gold or platinum, and some REEs are more common than base metals like lead, though they are generally only found as trace impurities instead of primary cations in minerals (Long et al., 2010). Minerals that do form with REE's as their primary cation are rarely found in high enough concentrations to be economically viable deposits. China is currently in control of >90% of the world's supply of REEs (Chen, 2011), presenting the potential for a supply problem. Understanding basic material

properties of REE bearing minerals such as the temperatures at which different phases are thermodynamically stable and how they respond to changes in temperature can assist in understanding how economically viable deposits might form, thereby assisting in the discovery of new deposits.

Having the general formula of $(Ce,La,Nd,Y)CO_3(F,OH)$, bastnaesite is the most common mineral mined for REEs. It occurs most often in carbonatites and is usually found in association with calcite, dolomite, and barite. Bastnaesite-(La) is the lanthanum fluoride end member ($LaCO_3F$) (Oftedal, 1931; Donnay and Donnay, 1953; Ni et al., 1993; Long et al., 2010; Castor, 2008a, 2008b). This work explores the ambient temperature behavior of bastnaesite-(La) at high pressure using single crystal X-ray diffraction in a diamond anvil cell.

Background

Structure of bastnaesite-(La)

Under ambient conditions, bastnaesite-(La) ($LaCO_3F$) exhibits hexagonal symmetry in the P-62c space group. Each unit cell contains six formula units of alternating layers of carbonate anions and layers of lanthanum cations and fluorine anions. The lanthanum-fluorine layers are parallel to the *a*- axis while the carbonate anion groups between them are locally parallel to the *c*-axis (Donnay and Donnay, 1953; Oftedal, 1931; Ni et al., 1993). See figure 3-1 for a structural model (Momma and Izumi, 2011).

Compressibility – the Birch-Murnaghan equation of state

The change in volume (ΔV) of a material due to modifications of thermodynamic state variables, such as temperature or pressure, is related to the free energy of the material, which

determines whether the material's structure is stable. Compressibility of a material can be described by an isothermal equation of state. The third order Birch-Murnaghan equation of state (Birch, 1947) describes a material's change in volume as a response to a change in hydrostatically applied pressure at a fixed temperature. It is represented by:

$$P(V_m) = \frac{3K_o}{2}\left[\left(\frac{V_o}{V_m}\right)^{\frac{7}{3}} - \left(\frac{V_o}{V_m}\right)^{\frac{5}{3}}\right] \times \{1 + \frac{3}{4}(K' - 4)[(\frac{V_o}{V_m})^{\frac{2}{3}} - 1]\}$$

Where P is hydrostatically applied pressure, V_m is the measured unit cell volume, and V_o is the unit cell volume measured at ambient pressure and temperature. K_o is the bulk modulus which describes a material's resistance to compression, or the ratio of the change in pressure to the reduction in volume and is represented by the expression:

$$K_o = -V(\frac{\partial P}{\partial V})_P$$

K` is the first derivative of the bulk modulus. For many materials at pressures below ~10 GPa, it is convenient to assume a value of K` = 4, which reduces the Birch-Murnaghan equation of state to its 2nd order form of:

$$P(V_m) = \frac{3K_o}{2}\left[\left(\frac{V_o}{V_m}\right)^{\frac{7}{3}} - \left(\frac{V_o}{V_m}\right)^{\frac{5}{3}}\right]$$

For many materials that only experience the pressure conditions found within the Earth's crust, this form is adequate to describe their behavior.

Methods

Synthesis

Bastnaesite-(La) was synthesized via precipitation from an aqueous solution at room pressure and temperature using the method described by Janka and Schleid (2009). Aqueous solutions of each reagent were made by mixing powdered lanthanum nitrate ($La(NO_3)_3 \bullet 6H_2O$, Sigma Aldrich 203548-100G, >99% purity), sodium bicarbonate ($NaHCO_3$, Sigma Aldrich S6014-25G, >99% purity), and sodium fluoride (NaF, Sigma Aldrich 201154-5G, >99% purity) with deionized water in separate beakers. The solutions were then combined in a larger beaker. Crystals of bastnaesite-(La) precipitate from the solution, with sodium nitrate ($NaNO_3$) remaining in solution. The fluid was decanted, and the bastnaesite-(La) precipitate was washed in deionized water and then centrifuged to remove any residual sodium nitrate. The powder was then dried in a Fischer Scientific model 289A Isotemp Vacuum oven under vacuum at 215°C for at least 12 hours.

Phase identification was completed by powder X-ray diffraction in a PANalytical X'Pert PRO and photoaccoustic infrared spectroscopy on a Digilab FTS-7000 Fourier transform infrared (FTIR) spectrometer. Reitveld structure refinement in X'pert Highscore Plus software was used to determine that the bastnaesite-(La) starting material contained <10% LaF_3 impurity. No OH peaks were detected in the FTIR spectra between 3600 and 3400 cm^{-1}.

The powder X-ray diffraction peaks from the synthesized bastnaesite-(La) are wide due to small particle size and or defects, so the material was next annealed in a Griggs modified piston cylinder apparatus as described by Tullis and Tullis (1986) using NaCl as the pressure transmitting medium. Samples were placed in a platinum jacket, surrounded by graphite, and sealed in a copper

capsule before being subjected to pressures between 0.25 and 1.0 GPa and temperatures from 700°C to 900°C. Figure 3-2 shows a comparison of diffraction patterns before and after annealing. The annealed material was lightly crushed in a mortar and pestle, and single crystals with diameters ~20 μm were separated under an optical microscope for synchrotron X-ray diffraction analysis.

Single crystal X-ray diffraction

In-situ single crystal synchrotron X-ray diffraction was performed at Sector 16 HPCAT of the Advanced Photon Source at Argonne National Laboratory. The pressure cells used were four-post diamond anvil cells (DAC) with 700 μm diameter culets and laser cut rhenium gaskets with 100 μm diameter gasket hole sample chamber. Single crystals of the annealed bastnaesite-(La) ~20 μm in diameter were placed in the sample chamber. Ruby spheres along with gold or copper powder were included in the sample chamber as pressure standards. The diamond cells were gas loaded (Rivers et al., 2008) with helium, neon, or argon as the pressure transmitting medium. Angular dispersive X-ray diffraction images were captured on a 2048x2048 pixel MAR CCD detector with a monochromatic beam of 30 KeV energy X-rays (λ=0.3738 nm) while rotating the DAC 30 degrees around the vertical axis. The ruby luminescence pressure scale (Mao et al., 1986) was used to estimate pressure during data collection and the equations of state for gold (Hirose et al., 2008) and copper (Wang et al., 2009) were used for final pressure determination. One DAC was placed in a vacuum chamber with kapton and mylar windows and equipped with resistive heating wires wound around the gasket between anvils and around the exterior of the DAC housing to generate and maintain sample chamber temperatures up to 400°C during data collection. Thermocouples were placed in contact with the diamonds to measure the sample temperature. Data analysis was completed using the software packages Fit2D (Hammersley, 2016), MDI Jade (Materials Data Inc), GSE_ADA/RSV (Dera et al., 2013), and EosFit7GUI (Angel et al., 2014).

Results

At ambient temperature, 16 X-ray diffraction patterns of bastnaesite-(La) were collected from ambient pressure to 11.3 GPa. Over this pressure range, the *a*- crystallographic axis contracts from 7.187 Å to 6.974 Å, the *c*- crystallographic axis contracts from 9.830 Å to 9.593 Å, with a corresponding unit cell volume contraction from 439.82 $Å^3$ to 404.06 $Å^3$. Table 3-1 lists the measured lattice parameters, calculated unit cell volumes, and crystallographic axis ratios for the corresponding pressure points. The unit cell volume data were fit to a third order Birch-Murnaghan equation of state (Birch, 1947; Angel et al., 2014) with V_o = 439.82 $Å^3$, K_o = 105 GPa, and K' = 5.58. Figure 3-3 illustrates the unit cell volume measurements superimposed over the EOS equation curve.

Over the elevated temperature range of 74°C to 400°C, 9 X-ray diffraction patterns were collected between 4.9 GPa and 7.7 GPa. Over this range of conditions, the *a*- crystallographic axis varies between 7.057 Å and 7.086 Å, the *c*- crystallographic axis varies between 9.730 Å and 9.685 Å, with corresponding variation in unit cell volumes between 423.11 $Å^3$ and 418.32 $Å^3$. Table 3-2 lists the measured lattice parameters, calculated unit cell volumes, and crystallographic axis ratios for their corresponding pressure and temperature points.

Discussion and conclusion

Bastnaesite-(La) is anisotropic when compressed, meaning that the *a*- crystallographic axis shrinks more than the *c*- crystallographic axis in response to increased pressure. The changing ratio in *a/c* is listed in table 3-1. As illustrated in figure 3-1, the carbonate ions are all planar in parallel with the *c*- crystallographic axis. This suggests that most of the compression is accommodated by

shrinking of the La-O and La-F bonds. This rigid body behavior of the CO_3^{2-} anions has been observed in other carbonates at high pressure (Ross and Reeder, 1992; Ross, 1997; Zhang and Reeder, 1999). Future work on other fluorocarbonates should be completed to determine how this behavior changes as a function of different cations, and whether OH^- anions replacing F^- anions in the hydroxybastnaesites has a similar effect.

Compressibility has not been measured for any other fluorocarbonate minerals, so a direct comparison of the properties of bastnaesite-(La) measured in this investigation to other materials with similar structure is not possible. Anderson and Nafe (1965) found that when comparing many compounds bulk moduli versus their specific ionic volumes, multiple trends emerged. Figure 3-4 displays their data, with more additional data for carbonate minerals from Knittle (1995), Merlini (2012), and Xu (2015). Anderson and Nafe (1965) identified a sulfide-selenide-telluride trend, an oxide trend, a fluorite trend, and an alkali-halide trend. However, these authors did not include any carbonates in their investigation, but by adding the data for the carbonates listed in Knittle (1995), there appears to be a separate carbonate trend (yellow line in figurer 3-4), but the hydroxycarbonates azurite and malachite do not lie on this trend. The values measured for bastnaesite-(La) in this study plot in a location where it could be interacting with the carbonate trend, the fluorite trend, or the oxide trend. Work on other fluorocarbonates needs to be completed in order to determine which of these trends bastnaesites follow, or if fluorocarbonates have a separate trend entirely. If the speculation above that bastnaesite-(La)'s compressional anisotropy is related to rigid body behavior and placement of the carbonate ions is correct, it is then likely that bastnaesites would follow the carbonate trend.

While some measurements were taken at elevated temperatures (listed in table 3-2), there is not enough data to fit a thermally modified equation of state capable of modeling changes in

compressibility due to temperature at high pressure. However, if we use Fei's thermal equation of state (Fei, 1995):

$$V(T) = V_0 \times e^{\left[a_0(T-298)+\frac{1}{2}a_1(T-298)^2+a_2\left(\frac{1}{T}-\frac{1}{298}\right)\right]}$$

and the measured thermal expansion coefficients for bastnaesite-(La) from chapter 2 (V_0 = 439.82 Å^3, a_0 = -1.68×10^{-5} K^{-1}, a_1 = 8.34×10^{-8} K^{-1}, and a_2 = 3.126 K^{-1}), we can input the measured temperatures from the elevated temperature experiments, substitute the resulting values for V_o in the Birch-Murnaghan equation of state fit in this work, and the calculated pressures agree well with those measured from the copper pressure standard via X-ray diffraction. Table 3-3 lists the measured temperature, measured unit cell volumes, measured pressures, and calculated pressures. Since the temperatures and volumes from the elevated temperature DAC experiments were not used in the fitting of Fei's thermal equation of state in chapter 2 or in the fitting of the Birch-Murnaghan equation of state in this chapter, these data show that the fit of both equations of state are valid.

Tables

Pressure (GPa)	*a* (Å)	Uncertainty	*c* (Å)	Uncertainty	V (Å^3)	Uncertainty	*a/c* ratio	Pressure media	Pressure standard
0.00	7.187	0.002	9.833	0.040	439.82	0.044	0.7309	n/a	n/a
0.53	7.169	0.003	9.811	0.003	436.68	0.009	0.7307	Ne	Au
1.35	7.148	0.003	9.806	0.003	433.91	0.008	0.7289	Ne	Au
1.39	7.159	0.001	9.763	0.003	433.32	0.006	0.7333	He	Cu
1.53	7.158	0.001	9.780	0.003	433.96	0.006	0.7319	He	Cu
1.69	7.150	0.002	9.787	0.004	433.30	0.008	0.7306	He	Cu
2.11	7.144	0.004	9.766	0.006	431.64	0.013	0.7315	Ne	Au
2.15	7.145	0.001	9.769	0.003	431.88	0.005	0.7314	He	Cu
2.82	7.129	0.001	9.751	0.003	429.18	0.005	0.7311	He	Cu
2.90	7.117	0.002	9.761	0.002	428.15	0.006	0.7291	Ne	Au
3.69	7.111	0.001	9.734	0.002	426.23	0.004	0.7305	He	Cu
3.87	7.095	0.003	9.738	0.003	424.53	0.009	0.7286	Ne	Au
6.47	7.051	0.003	9.694	0.003	417.38	0.009	0.7274	Ne	Au
8.34	7.014	0.003	9.663	0.003	411.65	0.009	0.7259	Ne	Au
10.60	6.973	0.003	9.632	0.003	405.59	0.009	0.7239	Ne	Au
11.31	6.974	0.004	9.593	0.003	404.06	0.011	0.7270	Ne	Au

Table 3-1: Bastnaesite-(La) measured lattice parameters, unit cell volumes, a/c crystallographic axis ratios, pressure transmitting media, and pressure standards from 0 to 11.3 GPa at ambient temperature.

Pressure (GPa)	Temp (°C)	*a* (Å)	Uncertainty	*c* (Å)	Uncertainty	V (Å^3)	Uncertainty	*a/c* ratio
4.9	74	7.086	0.001	9.730	0.002	423.11	0.005	0.7283
5.1	51	7.084	0.002	9.721	0.002	422.47	0.006	0.7287
5.8	100	7.076	0.002	9.696	0.002	420.44	0.006	0.7298
6.5	150	7.070	0.002	9.699	0.003	419.85	0.007	0.7289
6.7	200	7.060	0.002	9.691	0.002	418.32	0.006	0.7285
6.7	250	7.063	0.002	9.697	0.003	418.93	0.007	0.7284
7.0	300	7.057	0.002	9.713	0.003	418.91	0.007	0.7266
7.3	350	7.065	0.001	9.694	0.002	419.01	0.005	0.7288
7.7	400	7.064	0.002	9.685	0.002	418.53	0.006	0.7294

Table 3-2: Bastnaesite-(la) measured lattice parameters, unit cell volumes, and a/c crystallographic axis ratios from 4.9 to 7.7 GPa pressure and from 74°C to 400°C temperature. All elevated temperature measurements were taken using gas loaded argon as the pressure transmitting media, and all pressures measured using the copper (Cu) as the pressure standard.

Temp (°C)	V (Å3)	Measured P (GPa)	Calculated P (GPa)	Difference	Error
74	423.11	4.90	5.03	0.13	0.03
51	422.47	5.09	5.11	0.02	0.00
100	420.44	5.78	6.02	0.24	0.04
150	419.85	6.46	6.46	0.00	0.00
200	418.32	6.74	7.23	0.49	0.07
250	418.93	6.71	7.28	0.57	0.08
300	418.91	6.97	7.57	0.60	0.09
350	419.01	7.33	7.84	0.51	0.07
400	418.53	7.69	8.33	0.64	0.08

Table 3-3: List of heated experiments comparing measured pressure using the gold standard (Hirose et al., 2008) *versus calculated pressures using the Fei thermal EOS* (Fei, 1995) *parameters measured in chapter 2. Difference is calculated by subtracting the measured pressure from the calculated pressure. Error is calculated by dividing the difference by the measured pressure.*

Figures

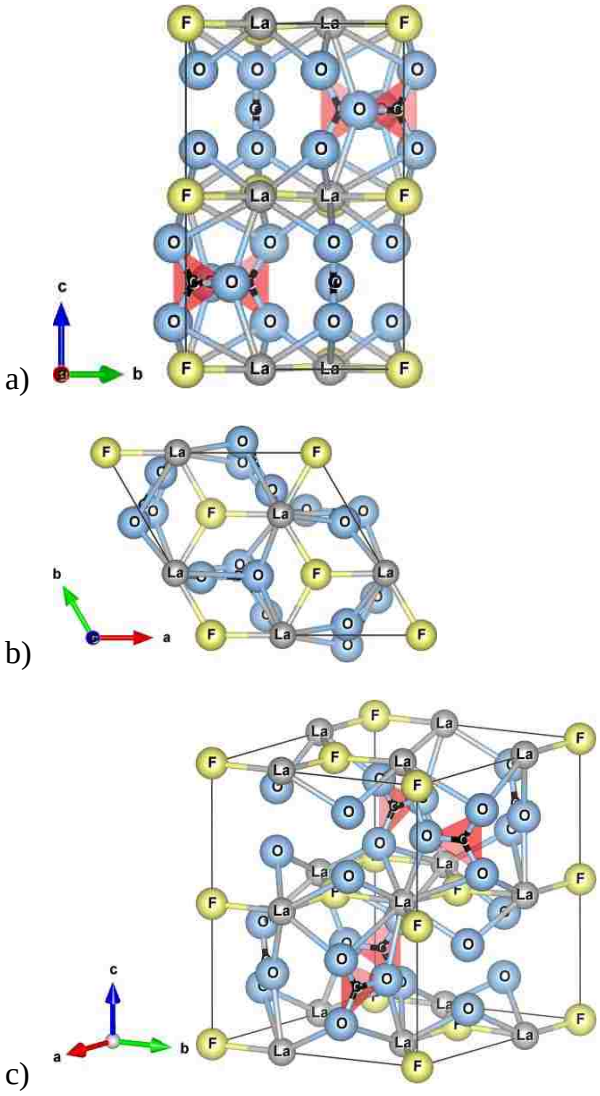

Figure 3-1: Structure of bastnaesite-(La) generated in the software VESTA (Momma and Izumi, 2011)*, a) as viewed down the a- axis, b) as viewed down the c- axis, and c) as viewed from an arbitrary angle* (Ni et al., 1993)*. In all three images, the trigonal planar polyhedral for the* CO_3^{2-} *ions are highlighted in red.*

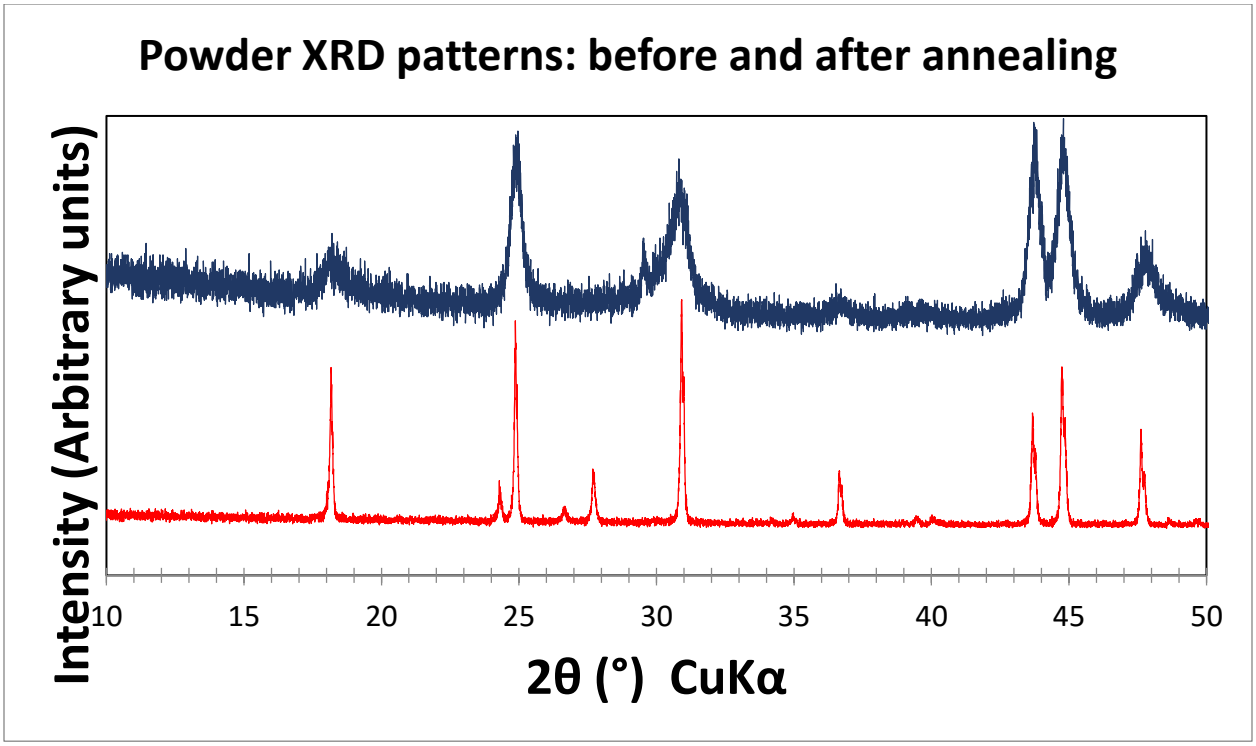

Figure 3-2: Powder XRD patterns of synthesized bastnaesite-(La) starting material. Top pattern is after washing and drying, bottom pattern is after annealing in the Griggs modified piston cylinder apparatus.

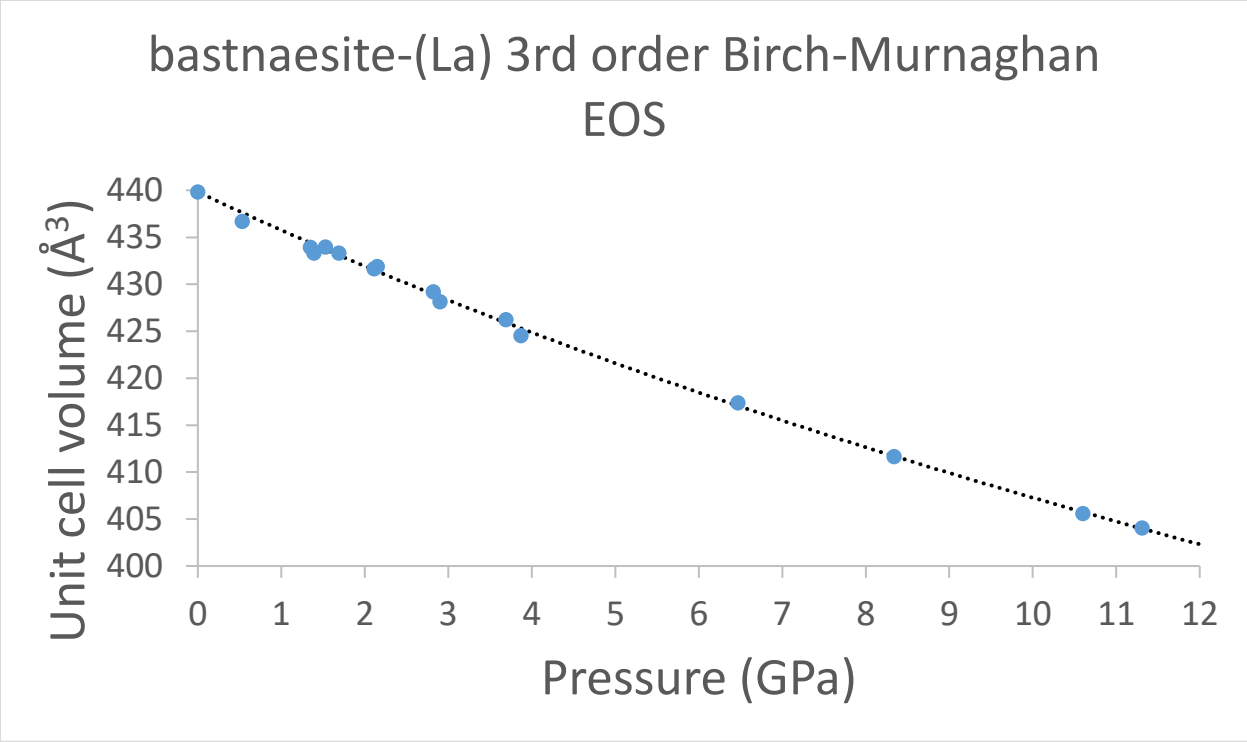

Figure 3-3: Pressure-volume data measured for bastnaesite-(La) fit to the 3rd order Birch-Murnaghan equation of state (Birch, 1947). *V_o=439.82 Å^3, K_o=105 GPa, K'=5.58. Blue circles are measured volumes from table 3-1, dotted line represents equation of state fit to data.*

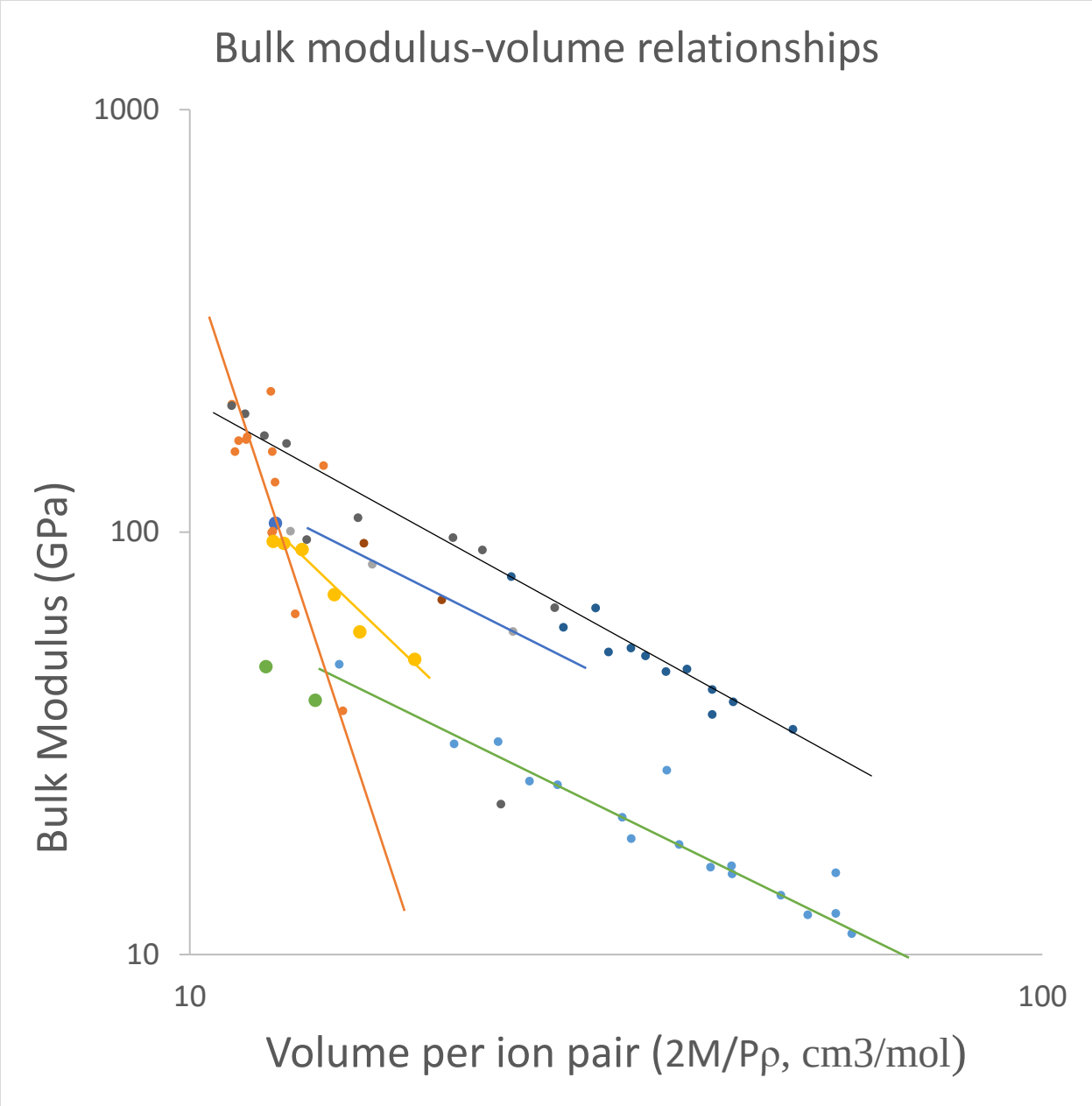

Figure 3-4: Bulk modulus versus specific volume for simple oxides, alkali halides, fluorites, sulfides, selenides, tellurides, and carbonates. Small dots include data from (Anderson and Nafe, 1965) *and* (Knittle, 1995). *Large blue dot is the values for bastnaesite-(La) measured in this study (2M/Pρ = 12.60 cm^3/mol, K_o = 105 GPa), large yellow dots are carbonates from* (Knittle, 1995), *and large green dots are malachite and azurite from* (Xu et al., 2015; Merlini et al., 2012). *Orange line is the oxide trend, black line is the sulfide, selenide, and telluride trend, blue line is the fluorite trend, green line is the alkali-halide trend, and yellow line is proposed carbonate trend.*

Chapter 4 – Phase equilibria of bastnaesite-(La)

Abstract

Understanding basic materials properties of rare earth element (REE) bearing minerals such as the temperatures and pressures at which different phases are thermodynamically stable and how they respond to changes in pressure or temperature can assist in understanding how economically viable deposits might form, thereby potentially leading to the discovery of new deposits. Bastnaesite is the most common REE bearing mineral mined. The lanthanum-rich end member, bastnaesite-(La), was synthesized and its behavior from ambient pressure to 1.2 GPa and temperatures up to 900°C was investigated in an oven and with a piston cylinder apparatus. A phase diagram illustrating this region of pressure and temperature space was constructed.

Introduction

Rare earth elements (REE), the elements from lanthanum to lutetium, are the first on the periodic table to begin populating f-block orbitals. They possess unique electronic and thus unique electronic properties and are sought after for technological applications for which other metals are not suitable. They are considered rare because they are generally only found as trace impurities instead of primary cations in minerals, not because of their relative abundances in rocks. Some REEs are more common in the crust than noble metals such as gold or platinum and base metals like lead. The minerals that do form with high REE content are rarely found in concentrations necessary for exploitable, economically viable deposits (Long et al., 2010). Currently, China controls >90% of the world's supply of REEs (Chen, 2011), presenting the potential for a supply problem. Understanding basic material properties of REE bearing minerals such as the

temperatures and pressures at which different phases are thermodynamically stable and how they respond to changes in temperature and pressure can assist in understanding how economically viable deposits might form, thereby potentially leading to the discovery of new deposits.

Having the general formula of $(Ce,La,Nd,Y)CO_3(F,OH)$, bastnaesite is the most common mineral mined for REEs. It occurs mainly in carbonatites and is usually found in association with calcite, dolomite, and barite. Bastnaesite-(La) is the lanthanum fluoride end member ($LaCO_3F$) (Oftedal, 1931; Donnay and Donnay, 1953; Ni et al., 1993; Long et al., 2010; Castor, 2008a, 2008b). This work explores the ambient pressure and high pressure thermal behavior of bastnaesite-(La) and the oxyfluorides it decomposes to using oven heating experiments and high pressure piston cylinder experiments.

Background

Structure and decomposition of bastnaesite-(La) to lanthanum oxyfluoride

Bastnaesite-(La) ($LaCO_3F$) exhibits hexagonal symmetry in the P-62c space group. Each unit cell contains six formula units of alternating layers of carbonate anions and layers of lanthanum cations and fluorine anions. The lanthanum-fluorine layers are parallel to the *a*- axis while the carbonate anion groups between them are locally parallel to the *c*- axis (Donnay and Donnay, 1953; Oftedal, 1931; Ni et al., 1993). See figure 4-1 for a structural model (Momma and Izumi, 2011). With the application of sufficient heat, bastnaesite-(La) decomposes via the decarbonation reaction $LaCO_3F$ + (heat) = LaOF + CO_2. At ambient conditions, γ-LaOF exhibits tetragonal symmetry in the P4/nmm space group with two formula units per unit cell (Woo et al., 2013; Jacob et al., 2006; Fergus and Chen, 2000; Shinn and Eick, 1969; Zachariasen, 1951). See figure 4-2 for a structural model. At high temperature, α-LaOF is stable with cubic symmetry in

the Fm-3m space group with four formula units per unit cell (Pistorius, 1973; Klemm and Klein, 1941; Mathews et al., 1997; Achary et al., 1998; Holtstam et al., 2004). See figure 4-3 for a structural model. β-LaOF is reported as stable at ambient pressure and temperature exhibiting rhombohedral symmetry in the R-3m space group with six formula units per unit cell (Achary et al., 1998; Woo et al., 2013; Zachariasen, 1951). I have not encountered this structure during this investigation.

Methods

Ambient pressure decomposition

Bastnaesite-(La) was synthesized via precipitation from an aqueous solution at room pressure and temperature using the method described by Janka and Schleid (Janka and Schleid, 2009). The details of the synthesis and phase identification processes were detailed in chapter 2 of this work. Synthetic bastnaesite-(La) starting material was packed into platinum crucibles and heated in an atmospheric pressure oven for approximately 24 hours each. Four experiments were conducted with 10°C increments, from 300°C to 330°C. Each sample was individually hand ground in a mortar and pestle and phases present were identified by powder X-ray diffraction in a PANalytical X'Pert PRO using X'pert Highscore Plus software.

High pressure decomposition

Samples of bastnaesite-(La) were subjected to high pressure and temperature in a Griggs-modified piston cylinder apparatus (Tullis and Tullis, 1986) using NaCl or Talc as the pressure transmitting medium and graphite as the furnace material. Oil pressure was measured using an Omegadyne pressure transducer on the hydraulic feed line to the main press ram. Sample

pressure was calculated by using the ratio of the inner surface of the ram over which the oil pressure acted to the surface area of the piston. No pressure correction was made for friction within the sample assembly, though previous piston cylinder work estimates pressure loss to be between 5-15%, (Mirwald et al., 1975), and up to half of the uncertainty may be ignored if the experiment is conducted with the piston cylinder apparatus in 'piston-in' configuration (Burnley and Getting, 2012). Samples were placed in a platinum jacket which was capped with an alumina disk but not sealed, surrounded by graphite, and sealed in a copper capsule. Samples were subjected to pressures ranging from of 0.2 to 1.2 GPa, and temperatures ranging from 700°C to 900°C for time between 4 and 24 hours. See figure 4-4 for a cross section of the sample assembly. Temperatures were measured using type S (Pt-Pt10%Rh) thermocouples. No correction was made for pressure effect on the EMF value measured from the thermocouples, as Lazarus et al. (1971) indicate that the largest correction that would be useful for a type S thermocouple is 0.06°C/GPa at 800°C, which is negligible, and Getting and Kennedy (1970) measured the error to be less than 9°C below 9 GPa. Experiments were quenched by removing power from the furnace assembly. Each sample was individually hand ground in a mortar and pestle and phases present were identified by powder X-ray diffraction in a PANalytical X'Pert PRO using X'pert Highscore Plus software.

Results

The temperature and pressure conditions, run duration, and resulting run products for every experiment in this investigation are listed in table 4-1. Under ambient pressure conditions, bastnaesite-(La) was stable in the experiments run at 300°C and 310°C, and γ-LaOF was observed in the experiments run at 320°C and 330°C. In piston cylinder experiments run at approximately 0.25 GPa, bastnaesite-(La) was found stable up to 800°C, and γ-LaOF was observed at 850°C. In

experiments conducted near 0.75 and 1.0 GPa, bastnaesite-(La) was found stable up to 850°C, and γ-LaOF was observed in experiments run at 900°C. The pressure, temperature, and phase information is illustrated in figure 4-5.

Discussion and conclusions

Phase diagram

The phase boundary or reaction line separating bastnaesite-(La) from its decomposition products (LaOF + CO_2) in figure 4-5 is represented with a dashed line because it is an estimate from decomposition reactions rather than from reversal experiments. The dashed line has been drawn as curved because CO_2 is a fluid phase, and at all conditions in this investigation it is above its critical temperature (38.1°C) (Tsuchiya et al., 2013). From the experimental data in table 4-1, there must be a change in slope of the phase boundary between ambient pressure and 0.25 GPa, because a straight line cannot be drawn between the bracketed experimental points. There is likely an invariant point along the phase boundary. As described in chapter 2 of this work, under ambient pressure conditions tetragonal γ-LaOF has a first order stuctural phase transition to cubic α-LaOF at 675°C. Additional work is needed to determine what effect pressure has on this phase transition. As discussed in chapter 2, with lower amounts of fluorine, the rhombohedral β-LaOF structure is stable in place of the tetragonal γ-LaOF (Achary et al., 1998). The temperature and pressure behavior of the α to β transition has been investigated up to 4 GPa; its ambient pressure temperature is 485°C (Pistorius, 1973), and has a steep enough slope that it would intersect our phase boundary below 0.25 GPa. This could also be a factor contributing to the change in slope of the bastnaesite-(La)-LaOF-CO_2 phase boundary below 0.25 GPa. The Grigg modified piston cylinder apparatus

isn't capable of investigating below this pressure, so other experimental techniques are needed to constrain this region of the phase diagram.

The ambient pressure experiments in this work found the decomposition temperature to be slightly lower than the differential scanning calorimetry and thermogravimetric analysis method from chapter 2; it was 310-320°C here and 325°C by the methods in chapter 2 of this work. While it is possible this could be accounted for due to the ±5°C error in temperature control for the oven used in this work, it is also possible that at this temperature range the rate of the decomposition reaction is too slow for the DSC/TGA apparatus to detect the reaction at the heating rates used, but the ~24 hour oven experiments had sufficient time. Further studies on the kinetics of the decarbonation reaction or slower heating rate DSC/TGA experiments could help address this inconsistency.

Calculation of phase boundary

A phase boundary in pressure and temperature space for a reversible reaction can be calculated if enough thermodynamic data for the phases involved in the reaction are known. The phase boundary is located where both the forward and reverse reactions are in equilibrium, which is also where the Gibbs free energy (ΔG) for the reaction is equal to zero. The equation for this can be approximated as:

$$\Delta G^{P,T} = \sum^{all\ phases} \left[H_f - TS + \int_0^T C_p\, dT - T \int_o^T \left(\frac{C_p}{T}\right) dT + \int_0^P \Delta V^{P,T} dT \right]$$

Where P is pressure, T is temperature in Kelvin, H_f is the enthalpy of formation of a phase from elements, S is the entropy of the reaction, C_p is the heat capacity of a phase at a given pressure,

and $\Delta V^{P,T}$ is the volume of a phase at a given pressure and temperature. By setting this equation equal to zero and iteratively solving for different pressure and temperature conditions, the phase boundary can be located (Ross and Navrotsky, 1987).

To calculate the phase diagram for the bastnaesite-(La)-LaOF-CO_2 system, some information is needed that is currently unavailable. H_f for bastnaesite-(La) has been measured as -1729.37$\pm$2.27 kJ/mol (Shivaramaiah et al., 2016), but C_p has not been measured. $\Delta V^{P,T}$ for bastnaesite-(La) can be approximated using the Birch-Murnaghan equation of state (Birch, 1947) fit in Chapter 3 of this work combined with the Fei thermal expansion equation of state (Fei, 1995) fit in chapter 2 of this work. H_f, C_p, and $\Delta V^{P,T}$ for γ-LaOF and α-LaOF are not available at the time of this writing, though the thermodynamic constants and equations of state for CO_2 are well characterized (Mäder and Berman, 1991). The entropy of reaction, S, can be approximated from the Clapeyron slope of the phase boundary. If all of the rest of the thermodynamic data and equations of state were known then by modifying the above Gibbs free energy equation to be cast as an inequality greater than or less than zero (depending upon which phases were found stable at a given pressure and temperature), it can be solved using a linear programming technique (Gordon, 1973). Once the needed thermodynamic data is available for bastnaesite-(La) and LaOF, this could be done with the information in table 4-3 and figure 4-5.

Tables

Experiment#	Pressure (GPa)	Temp (°C)	Duration	Pressure Media	Phase
RR_BAST_019a	0	300	23 hr 40 min	n/a	bastnaesite-(La)
RR_BAST_019b	0	310	24 hr 20 min	n/a	bastnaesite-(La)
RR_BAST_019c	0	320	27 hr 35 min	n/a	γ-LaOF
RR_BAST_019d	0	330	25 hr 5 min	n/a	γ-LaOF
RR_BAST_008	0.22	800	5 hr 7 min	NaCl	bastnaesite-(La)
RR_BAST_016	0.2	850	5 hr 3 min	Talc	γ-LaOF
RR_BAST_014	0.19	900	5 hr 2 min	Talc	γ-LaOF
RR_BAST_017	0.75	750	7 hr 4 min	NaCl	bastnaesite-(La)
RR_BAST_018	0.74	800	9 hr 35 min	NaCl	bastnaesite-(La)
RR_BAST_021	0.71	850	21 hr 3 min	NaCl	bastnaesite-(La)
RR_BAST_022	0.73	900	10 hr 57 min	NaCl	γ-LaOF
RR_BAST_015	1.21	820	4 hr 2 min	NaCl	bastnaesite-(La)
RR_BAST_010	0.96	850	5 hr 1 min	NaCl outer, Talc inner	bastnaesite-(La)
RR_BAST_011	0.98	900	5 hr 4 min	NaCl outer, Talc inner	γ-LaOF

Table 4-1: Conditions of experiments run as a part of this study and their end products as determined by powder X-ray diffraction.

Figures

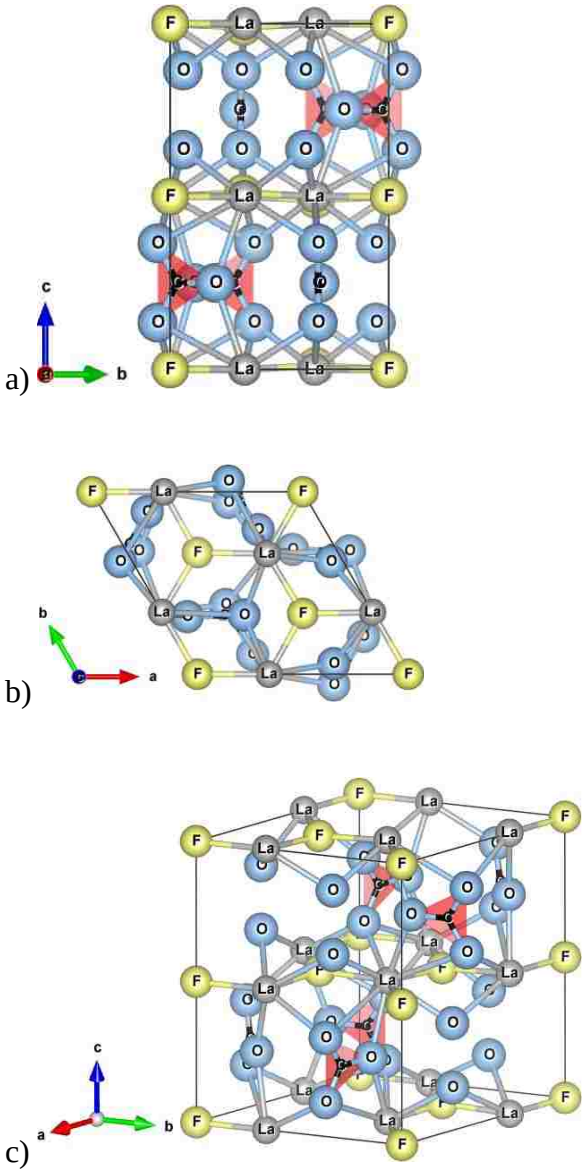

Figure 4-1: Structure of bastnaesite-(La) generated in the software VESTA (Momma and Izumi, 2011)*, a) as viewed down the a- axis, b) as viewed down the c- axis, and c) as viewed from an arbitrary angle* (Ni et al., 1993).

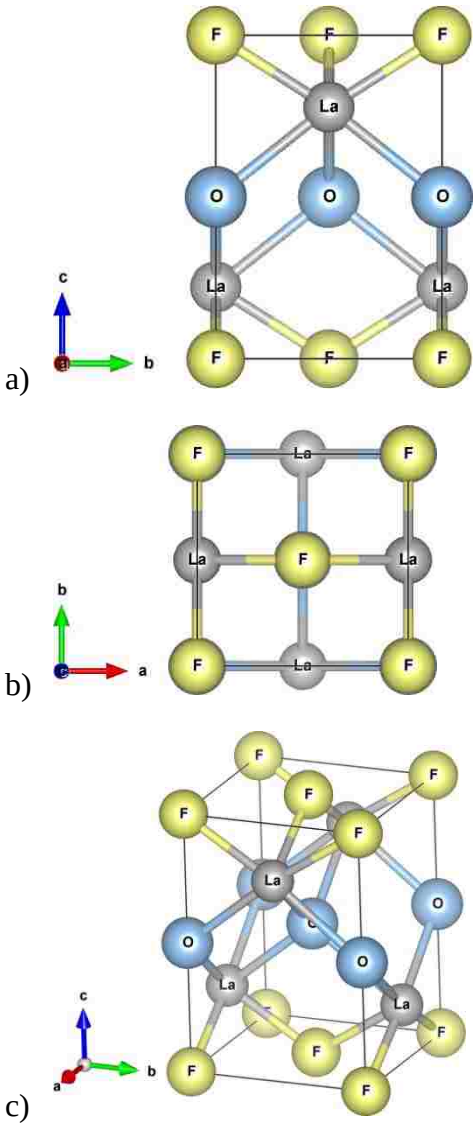

Figure 4-2: Structure of tetragonal γ-LaOF generated in the software VESTA (Momma and Izumi, 2011) a) as viewed down the a- axis, b) as viewed down the c- axis, and c) as viewed from an arbitrary angle (Zachariasen, 1951).

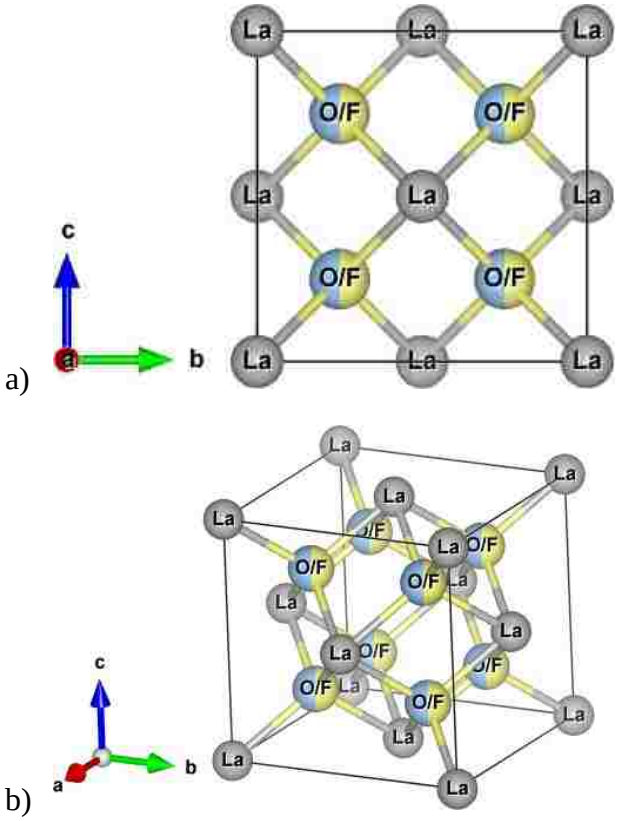

Figure 4-3: Structure of cubic α-LaOF generated in the software VESTA (Momma and Izumi, 2011) *a) as viewed down the a- axis, and b) as viewed from an arbitrary angle* (Holtstam et al., 2004).

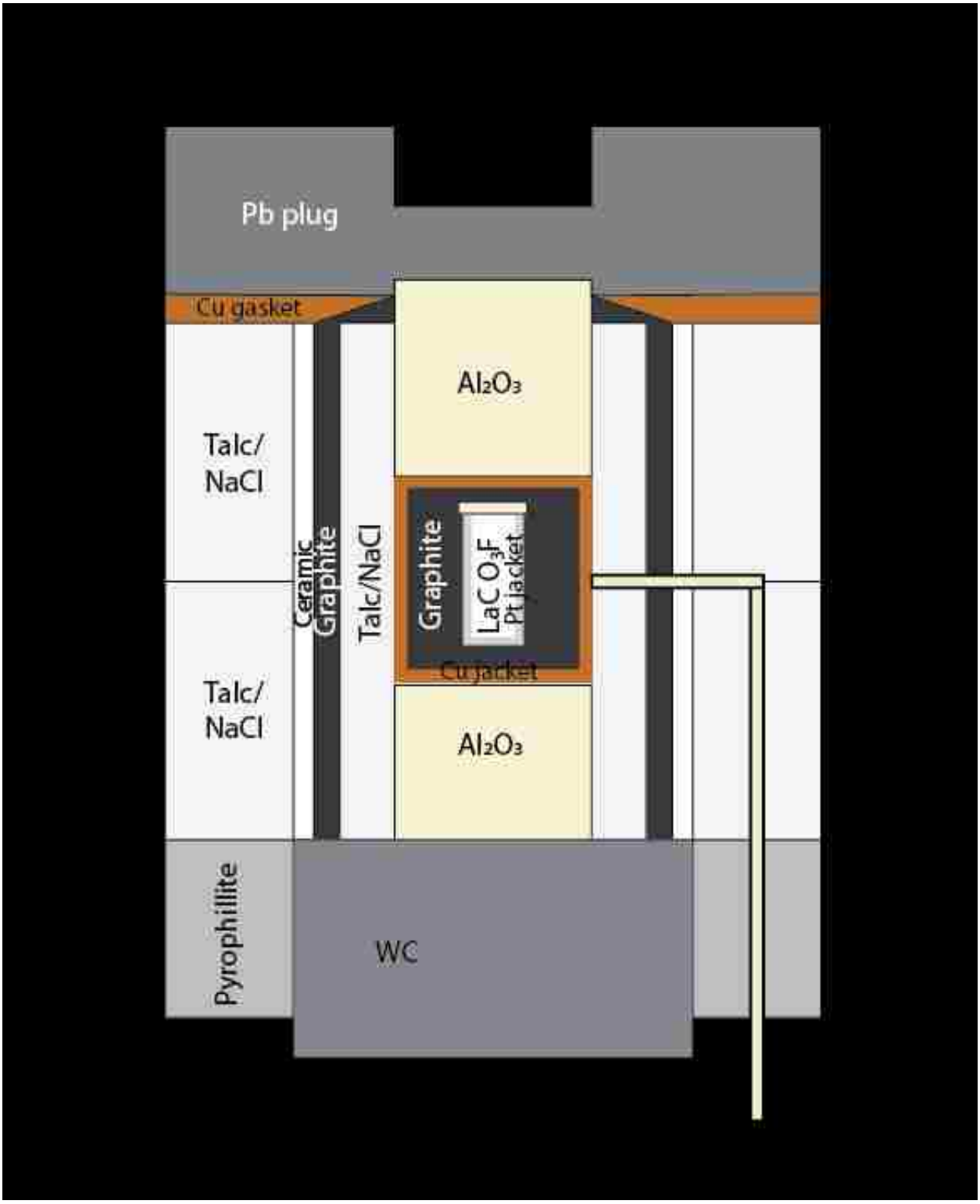

Figure 4-4: Drawing of sample assembly for high pressure and temperature decomposition experiments in the Griggs modified piston cylinder apparatus. The press apparatus design is described in Tullis and Tullis (1986).

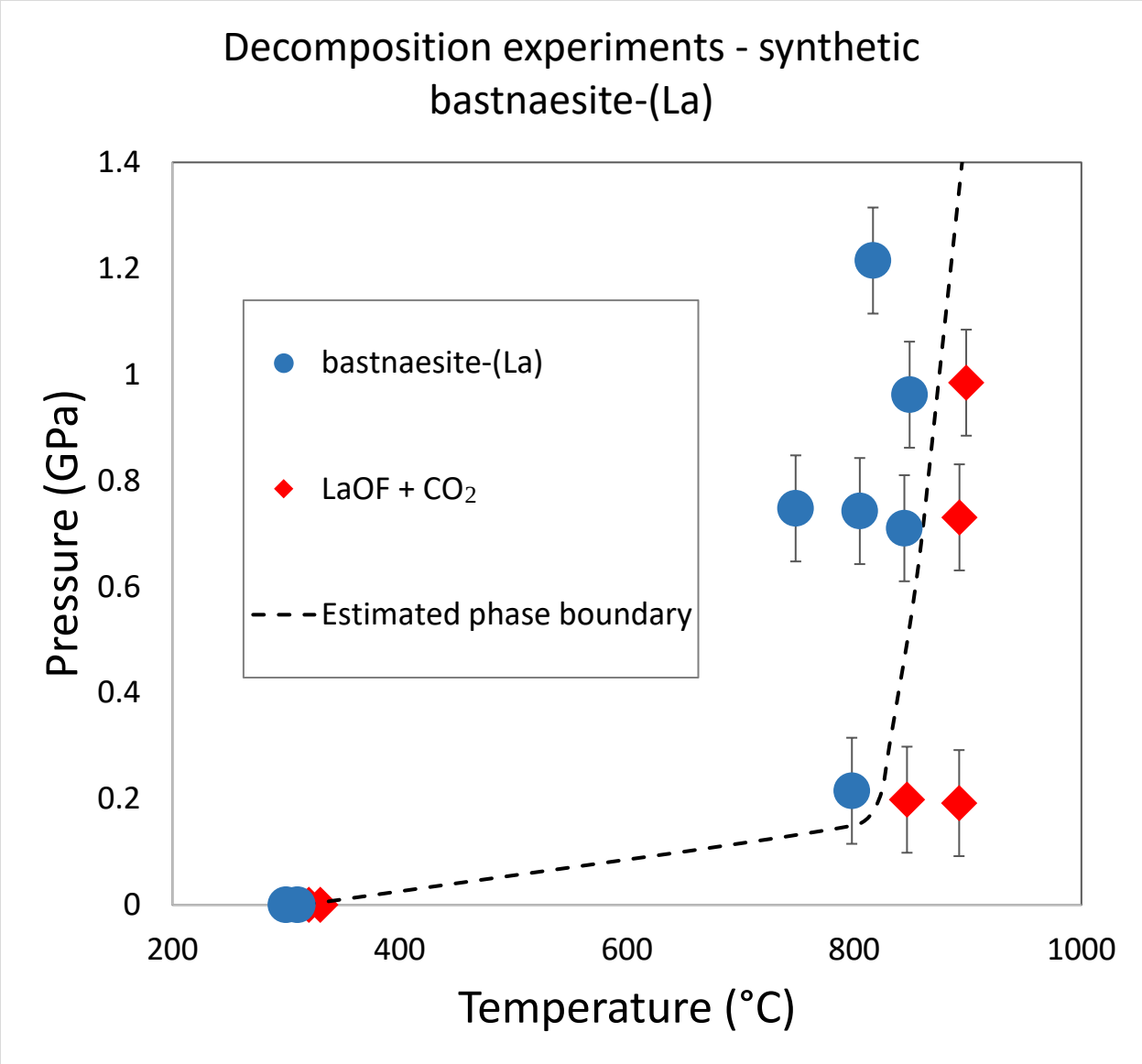

Figure 4-5: Phase diagram based upon bastnaesite-(La) decomposition experiments. Blue circles represent temperature and pressure conditions for experiments where bastnaesite-(La) was determined to be stable, and red diamonds represent temperature and pressure conditions for experiments where γ-LaOF was present. Black dashed line represents our estimation of the phase boundary location.

References

Achary, S.., Ambekar, B.., Mathews, M.., Tyagi, a. ., and Moorthy, P.., 1998, Study of phase transition and volume thermal expansion in a rare-earth (RE) oxyfluoride system by high-temperature XRD (RE=La, Nd, Sm, Eu and Gd): Thermochimica Acta, v. 320, p. 239–243, doi: 10.1016/S0040-6031(98)00449-3.

Altomare, A., Corriero, N., Cuocci, C., Falcicchio, A., Moliterni, A., and Rizzi, R., 2015, QUALX2.0: a qualitative phase analysis software using the freely available database POW_COD: J. Appl. Cryst., p. 598–603.

Anderson, O.L., and Nafe, J.E., 1965, The Bulk Modulus-Volume Relationship for Oxide Compounds and Related Geophysical Problems: JOURNAL OF GEOPHYSICAL RESEARCH, v. 70, doi: 10.1029/JZ070i016p03951.

Angel, R.J., Gonzalez-Platas, J., and Alvaro, M., 2014, EosFit7c and a Fortran module (library) for equation of state calculations: Zeitschrift fur Kristallographie, v. 229, p. 405–419, doi: 10.1515/zkri-2013-1711.

Birch, F., 1947, Finite Elastic Strain of Cubic Crystals: Physical Review, v. 71, p. 809–824.

Burnley, P.C., and Getting, I.C., 2012, Creating a high temperature environment at high pressure in a gas piston cylinder apparatus: Review of Scientific Instruments, v. 83, doi: 10.1063/1.3677844.

Castor, S.B., 2008a, Rare earth deposits of North America: Resource Geology, v. 58, p. 337–347, doi: 10.1111/j.1751-3928.2008.00068.x.

Castor, S.B., 2008b, The Mountain Pass rare-earth carbonatite and associated ultrapotassic rocks, California: Canadian Mineralogist, v. 46, p. 779–806, doi: 10.3749/canmin.46.4.779.

Chen, Z., 2011, Global rare earth resources and scenarios of future rare earth industry: Journal of Rare Earths, v. 29, p. 1–6, doi: 10.1016/S1002-0721(10)60401-2.

Dera, P., Zhuravlev, K., Prakapenka, V., Rivers, M.L., Finkelstein, G.J., Grubor-Urosevic, O., Tschauner, O., Clark, S.M., and Downs, R.T., 2013, High pressure single-crystal micro X-ray diffraction analysis with GSE_ADA/RSV software: High Pressure Research, v. 33, p. 466–484, doi: 10.1080/08957959.2013.806504.

Donnay, G., and Donnay, J.D.H., 1953, The Crystallography of Bastnaesite, Parisite, Roentgenite, and Synchisite: The American Mineralogist, v. 38, p. 932–963.

Fei, Y., 1995, Thermal Expansion, *in* Mineral physics and crystallography: a handbook of physical constants, p. 29–44.

Fergus, J.W., and Chen, H.P., 2000, Structure and Conductivity of Tetragonal and Rhombohedral Lanthanum Oxyfluoride Compounds: Journal of the Electrochemical Society, v. 147, p. 4696–4704.

Getting, I.C., and Kennedy, G.C., 1970, Effect of pressure on the emf of chromel-alumel and platinum-platinum 10% rhodium thermocouples: Journal of Applied Physics, v. 41, p. 4552–4562, doi: 10.1063/1.1658495.

Glass, J.J., and Smalley, R.G., 1945, Bastnäsite: The American Mineralogist, v. 30, p. 601–615.

Gordon, T., 1973, Determination of Internally Consistent Thermodynamic Data from Phase

Equilibrium Experiments: The Journal of Geology, v. 81, p. 199–208.

Gysi, A.P., and Williams-Jones, A.E., 2015, The thermodynamic properties of bastnäsite-(Ce) and parisite-(Ce): Chemical Geology, v. 392, p. 87–101, doi: 10.1016/j.chemgeo.2014.11.001.

Hammersley, A.P., 2016, FIT2D: A multi-purpose data reduction, analysis and visualization program: Journal of Applied Crystallography, v. 49, p. 646–652, doi: 10.1107/S1600576716000455.

Haschke, J.M., 1975, The lanthanum hydroxide fluoride carbonate system: The preparation of synthetic bastnaesite: Journal of Solid State Chemistry, v. 12, p. 115–121, doi: 10.1016/0022-4596(75)90186-3.

Hirose, K., Sata, N., Komabayashi, T., and Ohishi, Y., 2008, Simultaneous volume measurements of Au and MgO to 140 GPa and thermal equation of state of Au based on the MgO pressure scale: Physics of the Earth and Planetary Interiors, v. 167, p. 149–154, doi: 10.1016/j.pepi.2008.03.002.

Holland, T.J.B., and Redfern, S.A.T., 1997, Unit cell refinement from powder diffraction data: the use of regression diagnostics: Mineralogical Magazine, p. 65–77.

Holtstam, D., Grins, J., and Nysten, P., 2004, HÅLENIUSITE- (La) FROM THE BASTNÄS DEPOSIT , VÄSTMANLAND , SWEDEN : A NEW REE OXYFLUORIDE MINERAL SPECIES: v. 42, p. 1097–1103.

Hsu, L.C., 1992, Synthesis and Stability of Bastnaesites in a Part of the System (Ce, La)-F-H-C-

O: Mineralogy and Petrology, v. 47, p. 87–101.

Jacob, K.T., Saji, V.S., and Waseda, Y., 2006, Lanthanum oxyfluoride: Structure, stability, and ionic conductivity: International Journal of Applied Ceramic Technology, v. 3, p. 312–321, doi: 10.1111/j.1744-7402.2006.02086.x.

Janka, O., and Schleid, T., 2009, Facile synthesis of Bastnaesite-type LaF[CO3] and its thermal decomposition to LaOF for bulk and Eu3+-doped samples: European Journal of Inorganic Chemistry, p. 357–362, doi: 10.1002/ejic.200800931.

Klemm, V.W., and Klein, H.-A., 1941, Lanthanum Oxyfluoride: Zeitschrift fur anorganische und allgemeine Chemie, v. 248, p. 167–171.

Knittle, E., 1995, Static compression, *in* Mineral physics and crystallography: a handbook of physical constants, p. 98–142.

Lazarus, D., Jeffery, R.N., and Weiss, J.D., 1971, Relative pressure dependence of chromel/alumel and platinum/platinum- 10% rhodium thermocouples: Applied Physics Letters, v. 19, p. 371–373, doi: 10.1063/1.1653733.

Long, K.R., Van Gosen, B.S., Foley, N.K., and Cordier, D., 2010, The Principal Rare Earth Elements Deposits of the United States — A Summary of Domestic Deposits and a Global Perspective Gd Pr Sm Nd La Ce: US Geological Survey Scientific Investigations, v. 2010, p. 96, doi: 10.1007/978-90-481-8679-2_7.

Mäder, U.K., and Berman, R.G., 1991, An equation of state for carbon dioxide to high pressure and temperature: American Mineralogist, v. 76, p. 1547–1559.

Mao, H.K., Xu, J., and Bell, P.M., 1986, Calibration of the ruby pressure gauge to 800 kbar under quasi-hydrostatic conditions: Journal of Geophysical Research, v. 91, p. 4673, doi: 10.1029/JB091iB05p04673.

Markgraf, S., and Reeder, R., 1985, High-temperature structure refinements of calcite and magnesite: Am. Mineral., v. 70, p. 590–600.

Mathews, M.D., Tyagi, A.K., and Moorthy, P.N., 1997, Study of Phase Transition in REOF System by Dilatometry (RE = La, Nd, Sm, Gd, Eu and Y): Thermochimica Acta, v. 298, p. 165–167.

Merlini, M., Perchiazzi, N., Hanfland, M., and Bossak, A., 2012, Phase transition at high pressure in Cu2CO3(OH)2 related to the reduction of the Jahn–Teller effect: Acta Crystallographica Section B Structural Science, v. 68, p. 266–274, doi: 10.1107/S0108768112011226.

Mirwald, P.W., Getting, I.C., and Kennedy, G.C., 1975, Low-Friction Cell for Piston-Cylinder High-Pressure Apparatus Hard-fired Pyrophyllite Soft-fired Stainless Steel Boron Nitride Disk Lead Foil + MoS 2 Grease: Journal of Geophysical Research, v. 80, p. 1519–1525.

Momma, K., and Izumi, F., 2011, VESTA 3 for three-dimensional visualization of crystal, volumetric and morphology data: Journal of Applied Crystallography, v. 44, p. 1272–1276, doi: 10.1107/S0021889811038970.

Ni, Y., Hughes, J.M., and Mariano, A.N., 1993, The atomic arrangement of bastnasite-(Ce), Ce(CO3)F, and structural elements of synchysite-(Ce), rontgenite-(Ce), and parisite-(Ce): American Mineralogist, v. 78, p. 415–418.

Oftedal, I., 1931, Zur Kristallstruktur von Bastnasit, (Ce,La--)FCO3.: Zeitschrift fur Kristallographie, Kristallgeometrie, Kristallphysik, Kristallchemie, v. 78, p. 462.

Pistorius, C.W.F.T., 1973, Effect of Pressure on the Rhombohedral/Cubic Transitions of Some Lanthanide Oxide Fluorides: Journal of the Less-Common Metals, v. 31, p. 119–124.

Pradip, Li, C.C.H., and Fuerstenau, D.W., 2013, The Synthesis and Characterization of Rare-Earth Fluocarbonates: Kona, p. 193–200.

Rivers, M., Prakapenka, V., Kubo, A., Pullins, C., Holl, C., and Jacobsen, S., 2008, The COMPRES/GSECARS gas-loading system for diamond anvil cells at the Advanced Photon Source: High Pressure Research, v. 28, p. 273–292, doi: 10.1080/08957950802333593.

Ross, N.L., 1997, The equation of state and high-pressure behavior of magnesite: American Mineralogist, v. 82, p. 682–688.

Ross, N.L., and Navrotsky, A., 1987, The Mg2GeO4 olivine-spinel phase transition: Physics and Chemistry of Minerals, v. 14, p. 473–481, doi: 10.1007/BF00628825.

Ross, N.L., and Reeder, R.J., 1992, High-pressure structural study of dolomite and ankerite Ansrucr: American Mineralogist, v. 77, p. 412–421.

Sarge, S.M., Höhne, G.W.H., and Hemminger, W., 2014, Calorimetry: Fundamentals, Instrumentation, and Applications: John Wiley and Sons, Inc, 300 p.

Savko, K. a., and Bazikov, N.S., 2011, Phase equilibria of bastnaesite, allanite, and monazite: Bastnaesite-out isograde in metapelites of the Vorontsovskaya group, Voronezh crystalline massif: Petrology, v. 19, p. 445–469, doi: 10.1134/S0869591111030076.

Shinn, D.B., and Eick, H. a., 1969, Phase analyses of lanthanide oxide fluorides: Inorg. Chem., v. 8, p. 232–235, doi: 10.1021/ic50072a010.

Shivaramaiah, R., Anderko, A., Riman, R.E., and Navrotsky, A., 2016, Thermodynamics of bastnaesite: A major rare earth ore mineral: American Mineralogist, v. 101, p. 1129–1134, doi: 10.2138/am.2010.3521.

Tsuchiya, N., Sekiguchi, C., and Hirano, N., 2013, Spectroscopic Measurement of Critical Points and Characteristics of Supercritical State of H2O and CO2: Procedia Earth and Planetary Science, v. 7, p. 846–849, doi: 10.1016/j.proeps.2013.03.139.

Tullis, T.E., and Tullis, J., 1986, Experimental Rock Deformation Techniques: Geophysical Monograph, v. 36, p. 297–324.

Wang, Y., Zhang, J., Xu, H., Lin, Z., Daemen, L.L., Zhao, Y., and Wang, L., 2009, Thermal equation of state of copper studied by high P-T synchrotron x-ray diffraction: Applied Physics Letters, v. 94, p. 1–4, doi: 10.1063/1.3085997.

Woo, D.C., Lee, M.H., and Jung, W.S., 2013, Synthesis and characterization of rhombohedral- and tetragonal-lanthanum oxyfluoride powders: Ceramics International, v. 39, p. 1533–1538, doi: 10.1016/j.ceramint.2012.07.103.

Xu, J., Kuang, Y., Zhang, B., Liu, Y., Fan, D., Zhou, W., and Xie, H., 2015, High-pressure study of azurite Cu3(CO3)2(OH)2 by synchrotron radiation X-ray diffraction and Raman spectroscopy: Physics and Chemistry of Minerals, v. 42, p. 805–816, doi: 10.1007/s00269-015-0764-7.

Yang, H., Dembowski, R.F., Conrad, P.G., and Downs, R.T., 2008, Crystal structure and Raman spectrum of hydroxyl-bastnasite-(Ce), CeCO3(OH): American Mineralogist, v. 93, p. 698–701, doi: 10.2138/am.2008.2827.

Ye, Y., Smyth, J.R., and Boni, P., 2012, Crystal structure and thermal expansion of aragonite-group carbonates by single-crystal X-ray diffraction: American Mineralogist, v. 97, p. 707–712, doi: 10.2138/am.2012.3923.

Zachariasen, W.H., 1951, Crystal chemical studies of the 5 f -series of elements. XIV. Oxyfluorides, XOF: Acta Crystallographica, v. 4, p. 231, doi: 10.1107/S0365110X49000217.

Zhang, J., and Reeder, R.J., 1999, Comparative compressibilities of calcite-structure carbonates : Deviations from empirical relations: American Mineralogist, v. 84, p. 861–870.

Curriculum Vitae

Richard L. Rowland II

Email address: OppositeofRick@gmail.com

Education:

University of Nevada, Las Vegas
M.S., Geoscience, Expected December 2017
Thesis title: Phase equilibria, compressibility, and thermal analysis of bastnaesite-(La)
Committee: Pamela C. Burnley, Elisabeth M. Hausrath, Shichun Huang, Paul Forster

University of Nevada, Las Vegas
B.S., Geoscience, December 2014